

Multi-messenger emission derived from relativistic magnetized jet dynamics using a multi-zone framework

HARSHITA BHUYAN,¹ BHARGAV VAIDYA,¹ CHRISTIAN FENDT,² AND ADITYA SHARMA¹

¹*Department of Astronomy, Astrophysics and Space Engineering, Indian Institute of Technology Indore, India*

²*Max Planck Institute for Astronomy, Königstuhl 17, 69117 Heidelberg, Germany*

(Dated: March 2, 2026)

ABSTRACT

Relativistic jets from Active Galactic Nuclei (AGN) are highly energetic and emit radiation across a wide range of frequencies. Despite several observational studies, their particle composition still remains a key open question. The detection of high-energy neutrinos from blazar sources such as TXS 0506+056 has highlighted the plausibility of hadronic/lepto-hadronic models for AGN jets. To understand the origin of high-energy neutrinos from such sources, it is imperative to capture the complex interplay between the jet dynamics, their composition, and the mechanism of particle acceleration and cooling in relativistic jets. In this pilot study, we have coupled a numerical multi-zone framework for lepto-hadronic modeling, with 3D relativistic magneto-hydrodynamic simulations of AGN jets, including external photon fields. Our framework provides synthetic multi-wavelength and neutrino flux by spatially sampling the simulated jet into multiple zones. We investigate the implications of such a framework in exploring the different intrinsic and extrinsic pathways for proton-enrichment in jets. Essentially, we find that for low proton-to-electron number density ratios, producing a substantial jet neutrino flux, requires the underlying proton energy distribution to have a relatively flat spectrum with a power-law index of $\simeq 2.0$. We further find that while intrinsic shocks triggered by kink-instabilities in the jet can accelerate electrons to high energies, they may not be sufficient to produce such flat particle energy distributions for the chosen set of parsec-scale jet parameters. Finally, to produce a significant jet neutrino emission, our simulations suggest the need to consider particle acceleration mechanisms through alternative pathways, either internal or external.

Keywords: Relativistic jets, Multi-zone modeling, High-energy neutrinos

1. INTRODUCTION

Active Galactic Nuclei (AGN) launch highly collimated relativistic jets, which can be observed over a wide range of length scales (from pc to Mpc). Radiation emitted by these outflows, are predominantly non-thermal, encompassing almost the entire electromagnetic spectrum. AGN jet plasma, propagating with bulk Lorentz factors ranging from a few up to ~ 50 (Lister et al. 2009) and threaded by magnetic fields, gives rise to a range of small and large-scale structures, which are causally associated with variability timescales spanning a range from minutes to years (Hovatta & Lindfors 2019). Recent high-resolution radio imaging and multi-wavelength/messenger campaigns are aiding in unraveling the conditions under which these jets form, evolve and produce the observed emissions (e.g., Walker et al.

2018; Böttcher 2019; Blandford et al. 2019; Lister et al. 2021, and references therein).

Blazars are a class of AGN with jets oriented close to the line of sight of the observer. The Spectral Energy Distribution (SED) of blazars consists of two distinctly separated non-thermal peaks (the double hump structure). The first peak lies between the infrared and X-ray frequencies, the second peak lies between the MeV to TeV range in the gamma ray band (Urry 1999; Ghisellini & Tavecchio 2008; Abdo et al. 2010). Although the low-frequency peak has a well-established origin, the mechanisms driving the emissions contributing to the second peak are still a mystery. The source of this high energy peak of the blazar SED, at its core is a problem fundamentally associated with the composition of the AGN jet which remains elusive till date, and is an open question in astrophysics.

Different models have been proposed in order to probe into the matter composition of the jet, starting from leptonic models (Maraschi et al. 1992; Dermer & Schlickeiser 1993; Bloom & Marscher 1996; Błażejowski et al. 2000; Diltz & Böttcher 2014), to hadronic/lepto-hadronic models (Mastichiadis & Kirk 1995a; Mücke et al. 2003; Aharonian 2000; Böttcher et al. 2013; Murase et al. 2014; Cerruti et al. 2015; Petropoulou et al. 2015; Zacharias et al. 2022). These models incorporate various acceleration and radiative cooling mechanisms relevant to the particle species they propose as constituents of the jet. While all of these models can replicate the observed electromagnetic emissions from blazars, neutrino production is exclusive to models involving hadrons.

In September 2017, the IceCube Neutrino Observatory detected a ~ 290 TeV neutrino, from a direction consistent with the blazar TXS 0506+056. This triggered a follow-up analysis of 9.5 years of archival IceCube data, which revealed an excess of 13 ± 5 muon neutrinos from the same direction during the 2014 - 2015 period, with a significance of 3.5σ (Aartsen et al. 2018). Further, Baikal GVD also detected a neutrino event from this blazar source in 2021 (Allakhverdyan et al. 2023). Additionally, PKS B1424-418 (Kadler et al. 2016), GB6 J1040+06170617 (Garrappa et al. 2019), and PKS 0735+178 (Sahakyan et al. 2022; Omeliukh et al. 2025) are other blazar sources identified as possible candidates for neutrino events detected in IceCube. Evidence demonstrating that neutrinos are statistically associated with radio-bright blazars have been shown by utilizing a total of 71 track like IceCube events from 2009 - 2022 (Plavin et al. 2020; Plavin et al. 2021, 2023). In subsequent analysis of IceCube archival data for different AGN sources, a substantial neutrino excess was found from a Seyfert galaxy NGC 1068 as well, with a 4.2σ significance (Abbasi et al. 2022). These observations have naturally reignited the interest in hadronic and lepto-hadronic models for AGN jets as unlike their purely leptonic counterparts, they can account for neutrino production.

High-energy neutrino production in AGN jets requires proton acceleration to very high energies, enabling photo-meson and proton-proton (pp) interactions. These interactions initiate hadronic cascades through the decay of charged pions and muons, ultimately producing neutrinos with a characteristic flavor ratio of $\nu_e : \nu_\mu : \nu_\tau = 1 : 2 : 0$ at the source (Zuber 2020). Neutrino oscillations over huge cosmological distances effectively average out, gradually transforming the initial flavor ratio during propagation to an arrival ratio of $1 : 1 : 1$ (Aartsen et al. 2015).

Particle acceleration in AGN jets may arise either through internal shocks driven by jet dynamics and fluid instabilities (for e.g. Marcowith et al. 2020, and references therein), or via external shocks created as the jet interacts with its surroundings (Barkov et al. 2012; del Palacio, S. et al. 2019; Britzen et al. 2019). Several state-of-the-art particle acceleration models have also been developed in the last few years to study non-thermal emission from relativistic jets (Liu et al. 2017; Matthews et al. 2020; Kundu et al. 2021; Upreti et al. 2024; Dubey et al. 2023; Jerrim et al. 2025). Specifically, in the case of accelerating hadrons, additional mechanisms like magnetic reconnection (Giannios 2010; Ball et al. 2018; Fiorillo et al. 2024) and the espresso mechanism (Mbarek & Caprioli 2021) can also contribute significantly, potentially leading to ultra-high-energy cosmic-ray (UHECR) and neutrino production. This raises a key question: is the hadronic component (if any) in neutrino-emitting blazars an intrinsic part of the jet, or is it entrained from the surrounding medium through jet-environment interactions?

To disentangle the question above, it is important to capture the intricate relationship between jet composition, its interactions and dynamical behaviour, and the microphysics governing particle transport. This is a task where computational simulations can serve as indispensable tools.

Throughout the years, there have been a few attempts to computationally implement the Blazar lepto-hadronic models. Some of the noteworthy implementations include the AM3 code (Gao et al. 2017), ATHE ν A (Mastichiadis & Kirk 1995b; Petropoulou et al. 2014), Böttcher13(B13) (Böttcher et al. 2013), LeHa-Paris (Cerruti et al. 2015), and *Katu* (Jiménez-Fernández & van Eerten 2020). A common feature among most of these lepto-hadronic codes is that they are typically utilized for single emission zone modeling, which assumes that the majority of emissions from an AGN jet are arising from a single homogeneous emission region. On the other hand, there are multi-zone models (Xue et al. 2021; Aguilar-Ruiz et al. 2023), which advocate for the possibility of multiple emission regions inside the jet contributing to the observed emissions.

Most lepto-hadronic codes however do not incorporate the dynamical evolution of the jet, ignoring how the interplay of various phenomena like shocks, instabilities and magnetic reconnection across the jet can produce several regions where different particle acceleration and cooling processes may dominate resulting in multiple emission zones that may significantly impact the observed emissions. These multi-zone models, despite being a more realistic representation of the actual physics

happening inside AGN jets, are challenging to implement due to their complexity as well as an extensive free-parameter space. Hence, only a limited number of studies have utilized these models to successfully explain the observed multi-wavelength and neutrino emissions coming from different blazar jets. Xue et al. (2021) is one such study which uses a two zone approach, whereas Zacharias et al. (2022) explores a lepto-hadronic model for an extended jet.

To address these notable challenges in modeling AGN jets and its emissions, in this study we introduce a computational framework for lepto-hadronic multi-zone modeling that builds upon the foundation of existing codes that are suitable for one-zone modeling. In this unique approach, we couple the multi-zone framework with 3D relativistic magneto-hydrodynamic (RMHD) simulations with particle transport, to draw inference about the free parameters for each emission zone in the jet. This reduces the huge free parameter space typically required for multi-zone modeling.

Hence, our multi-zone framework essentially acts as a bridge between dynamical simulations and microphysics of particle evolution within the jet. This can serve as a virtual testbed to model and study different extrinsic and intrinsic scenarios for proton enrichment in jets and its subsequent multi-messenger emissions. For the purposes of this study, we restrict our focus to exploring the emissions from a particle population intrinsic to the jet, the extrinsic scenarios will be explored in our subsequent works.

This paper is organized as follows. In Section 2, we describe the numerical setup and outline the methodology behind our multi-zone framework. Section 3 presents the key results for two jet simulations differing in initial bulk Lorentz factor, together with the outcomes from their multi-zone analyses. In Section 4 we discuss the implications of our findings, and present the conclusions in Section 5.

2. NUMERICAL APPROACH

In this section we delve into the numerical setup for our lepto-hadronic multi-zone framework. We will explain in details the methodology we use to integrate the dynamical evolution of the relativistic jet with this framework in order to model the photon SED and neutrino flux. We will also elaborate on the two computational codes we utilize for our work, along with the initial parameters and the boundary conditions used for the simulation setup.

2.1. Dynamical modeling

For this work, we utilize the PLUTO code (Mignone et al. 2007), a multi-algorithm fluid dynamics code, to

perform 3D RMHD simulations for a section of an AGN jet. Performing such simulations involve numerically solving the following system of equations in its conservative form,

$$\frac{\partial}{\partial t} \begin{pmatrix} \Gamma\rho \\ \mathbf{m} \\ \mathcal{E}_t \\ \mathbf{B} \end{pmatrix} + \nabla \cdot \begin{pmatrix} \Gamma\rho\mathbf{v} \\ w_t\Gamma^2\mathbf{v}\mathbf{v} - \mathbf{b}\mathbf{b} + Ip_t \\ \mathbf{m} \\ \mathbf{v}\mathbf{B} - \mathbf{B}\mathbf{v} \end{pmatrix}^T = 0, \quad (1)$$

where ρ is the rest-mass density, \mathbf{v} is the bulk velocity, Γ is the bulk Lorentz factor, and I is the identity matrix. Here, \mathbf{B} is the observer frame magnetic field while the co-moving frame magnetic field is given by $b^k = \Gamma \{ \mathbf{v} \cdot \mathbf{B}, B^i/\Gamma^2 + v^i(\mathbf{v} \cdot \mathbf{B}) \}$, the relativistic total enthalpy is $w_t \equiv (\rho h + b^2)$, $\mathbf{m} = w_t\Gamma^2\mathbf{v} - b^0\mathbf{b}$ is the momentum density, $\mathcal{E}_t = w_t\Gamma^2 - b^0b^0 - p_t$ represents the total energy density, and $p_t = P + b^2/2$ is the total pressure where P is the gas pressure (Del Zanna et al. 2003; Mignone & McKinney 2007).

2.1.1. Numerical setup

We model a representative section of an AGN jet, taking a cylindrical plasma column with an initial radius of $R_j \equiv l_0 = 1$ pc, in which the material propagates along the z-axis. We apply a uniform 3D Cartesian grid. The size of the entire simulation domain is $[-L_x < x < L_x]$, $[-L_y < y < L_y]$, and $[0 < z < L_z]$, where $L_x = L_y = L_z = 24l_0 = 24$ pc. The domain numerical grid has $(768 \times 768 \times 384)$ grid cells resulting in a resolution of 16 cells per pc. Therefore, the simulation domain represents a parsec-scale segment of the AGN jet, capturing the jet's early propagation phase near the broad-line region and the central engine.

All the quantities in our dynamical simulations are defined in dimension-less code units, with density being scaled by $\rho_0 = 1.661 \times 10^{-26}$ g cm⁻³, magnetic field being scaled by $B_0 = v_0\sqrt{4\pi\rho_0} = 0.014$ G, while $P_0 = \rho_0v_0^2 = 1.492$ dyne cm⁻² and $t_0 = l_0/v_0 = 3.26$ years are used to normalize pressure and time respectively. Velocities are normalized to the speed of light, $v_0 = c$.

We apply a divergence cleaning algorithm prescribed to preserve the $\nabla \cdot \mathbf{B} = 0$ condition (Dedner et al. 2002). A total variation diminishing (TVD) piece-wise linear reconstruction scheme (Mignone 2014) which is 2nd order accurate in space, has been used for the primitive variables along with a second order accurate Runge-Kutta algorithm for time stepping. Additionally, we have adopted the Taub-Matthews equations of state as defined in Mignone & McKinney (2007) to close the respective conservation laws in Equation 1.

2.1.2. Initial conditions and boundary conditions

We assume a rotating, inviscid, infinitely conducting flow constituting our jet. The jet section is initialized as an axisymmetric cylindrical plasma column by prescribing radial profiles of various flow variables following Bodo et al. (2019). Choosing the Lorentz factor $\Gamma_z(r)$ profile of the form

$$\Gamma_z(r) \equiv \frac{1}{\sqrt{1-v_z^2}} = 1 + \frac{\Gamma_c - 1}{\cosh(r/r_j)^6}, \quad (2)$$

where, Γ_c is the Lorentz factor along the central axis, r_j is the jet radius, and v_z is the axial velocity. The azimuthal velocity v_ϕ , toroidal (B_ϕ) and poloidal magnetic field (B_z) profiles taken for our simulations are defined in Appendix A. To trigger the onset of current-driven instabilities, a perturbation following the formulation specified in Rossi et al. (2008) is applied to the radial velocity. The corresponding expression can be defined as

$$v_r = \frac{K_0}{24} \sum_{m=0}^2 \sum_{l=1}^8 \cos(m\phi + \omega_l t + o_l), \quad (3)$$

which sums up waves of different frequencies with $\omega_l = c_s(0.5, 1, 2, 3, 0.03, 0.06, 0.12, 0.25)$. This considers different jet instabilities with $m = 0, 1, 2$ representing sausage, kink and fluting modes respectively. The o_l represents random phase shifts and the amplitude K_0 denotes the fractional change of the bulk Lorentz factor given by $K_0 = \frac{\sqrt{(1+\psi)^2-1}}{\Gamma(1+\psi)}$, where ψ is a small dimensionless parameter characterizing the relative strength of the perturbation, typically set to a value of 0.05.

We perform jet column simulations for two different initial bulk Lorentz factors along the central axis: $\Gamma_{c,\text{ini}} = 5, 10$. For both simulations, the initial density inside the jet column is defined as $\rho_j = \rho_0$, while ambient medium density is $\rho_a = 1000 \rho_0$. Initially, the pressure is taken to be uniform across the domain $P_j = P_a = 0.1 P_0$. To completely specify the magnetic field profiles, we define the pitch parameter along the central axis

$$\mathcal{P}_c = \left| \frac{r B_z}{B_\phi} \right|_{r=0}. \quad (4)$$

We apply $\mathcal{P}_c = 0.9$ for both jet simulations, while the central axis poloidal magnetic field B_{zc} and the jet angular velocity along the central axis Ω_c are different with values specified as,

- $B_{zc} = 1.710 B_0$, $\Omega_c = 0.434$ (for $\Gamma_{c,\text{ini}} = 5$),
- $B_{zc} = 2.148 B_0$, $\Omega_c = 0.192$ (for $\Gamma_{c,\text{ini}} = 10$).

The initial profiles defined in cylindrical coordinates are subsequently transformed into Cartesian coordinates to initialize the 3D Cartesian simulation grid.

To track the evolution of the jet material, we also define a tracer variable \mathcal{T} such that initially $\mathcal{T} = 1$ for the material in grid cells inside the jet, and $\mathcal{T} = 0$ for the ambient medium. To avoid sharp transitions or discontinuities at the jet boundary, each fluid variable is multiplied by a smoothening function.

Standard outflow boundary conditions are applied along the x and y direction vertical boundaries. The simulation domain is sufficiently large, placing these boundaries far enough from the jet core to prevent spurious reflections from influencing the solution. Periodic boundary conditions are imposed on the transverse planes at $z = 0$ and $z = 24 l_0$, which define the domain boundaries along the z -axis.

2.2. Hybrid particle module

The Lagrangian particle module for PLUTO code as described in Vaidya et al. (2018), utilizes a hybrid approach for modeling leptonic particles within fluid simulations, and its respective non-thermal emissions. It utilizes the concept of a Lagrangian macro-particle which is an ensemble of leptons in spatial proximity but with a finite distribution over an energy range. The macro-particles propagate through an Eulerian grid and get advected with the flow.

For each macro-particle, a time-dependent distribution function $N_{\text{LP}}^e(\gamma, \tau)$ can be defined, representing the number density of electrons over an energy range¹ For numerical convenience, we define a normalized number density ratio function χ_{LP}^e for the Lagrangian macro-particles such that:

$$\chi_{\text{LP}}^e(\gamma, \tau) = \frac{N_{\text{LP}}^e(\gamma, \tau)}{n_{\text{F}}}, \quad (5)$$

where n_{F} represents the fluid number density at the location of the macro-particle, γ represents the energy of the particle normalized to its rest mass energy, and τ is the proper time which is related to the lab-frame time t by $d\tau = dt/\gamma$.

It is important to note that, all the variables are defined in the co-moving frame unless explicitly stated otherwise, a convention which will be followed throughout the text.

A simplified form of the cosmic ray transport equation, derived under the assumptions specified in Vaidya et al. (2018), is used to describe the spatial and temporal evolution of Lagrangian macro-particles and the associated number density distribution function of the

¹ Subscript LP denotes the variables specified for Lagrangian particles, while superscripts e or p denote the particle species consisting of electrons/leptons or protons, respectively.

non-thermal particles within it. This particular form of the transport equation can be expressed as

$$\frac{d\chi_{\text{LP}}^e}{d\tau} + \frac{\partial}{\partial\gamma} \left[\left(-\frac{\gamma}{3} \Delta_\mu u^\mu + \dot{\gamma}_l \right) \chi_{\text{LP}}^e \right] = 0, \quad (6)$$

where $\dot{\gamma}_l < 0$ represents the radiative losses of the particles. The first term within the brackets accounts for the energy losses caused by adiabatic expansion. The particle module solves Equation 6 separately for the spatial and energy dependent parts.

The transport step handles the update of the spatial coordinates \mathbf{x}_{LP} for each macro-particle using the equation

$$\frac{d\mathbf{x}_{\text{LP}}}{dt} = \mathbf{v}(\mathbf{x}_{\text{LP}}), \quad (7)$$

where $\mathbf{v}(\mathbf{x}_{\text{LP}})$ is the interpolated fluid velocity at the position of the Lagrangian particle. This equation is solved consequently with the respective fluid equations.

This is followed by the spectral evolution step which governs the evolution of the particle distribution inside each macro-particle. Radiative losses of the particles via processes like synchrotron and Inverse Compton (Khangulyan et al. 2014; Acharya et al. 2023, Sharma et. al. in prep), as well as energy gains due to acceleration processes such as diffusive shock acceleration (see Section 2.2.1), are incorporated within the particle module.

The target photon field required for the inverse Compton losses may originate from various regions around the central supermassive black hole (SMBH), such as the broad line region (BLR), the accretion disk or the dusty torus (DT). In this study, for two of the simulations, we adopt simplified external photon fields for our jet, considering that in the AGN frame, the dissipation region is at a distance of $\gtrsim 10$ pc from the SMBH (assuming an opening angle of $\approx 2-4^\circ$). In particular, we consider a BLR field in one EC simulation and a DT field in the other. The BLR and DT radiation fields are approximated as blackbody radiation peaking respectively at frequencies $\approx 2 \times 10^{15}$ Hz (Ghisellini & Tavecchio 2008), and $\approx 3 \times 10^{13}$ Hz (Cleary et al. 2007) in the AGN frame. The corresponding AGN frame photon-field luminosities are parameterized as $L_{\text{BLR/DT}}^{\text{AGN}} = \mathcal{G}_{\text{BLR/DT}} L_{\text{disc}}^{\text{AGN}}$, where we adopt $L_{\text{disc}}^{\text{AGN}} = 6 \times 10^{45}$ erg s $^{-1}$ and covering factors $\mathcal{G}_{\text{BLR}} \approx 0.1$ and $\mathcal{G}_{\text{DT}} \approx 0.5$.

We use the approximation provided in Schlickeiser & Ruppel (2010) for the inverse Compton electron energy loss rate for an isotropic graybody photon field in the Klein-Nishina limit which can be expressed as follows,

$$|\dot{\gamma}_{\text{EC}}| \approx \frac{4\sigma_{\text{T}}cU_{\text{rad}}\gamma^2}{3m_e c^2} f_{\text{KN}}(\gamma) \quad (8)$$

where the subscript EC represents external Compton losses in our system, $f_{\text{KN}}(\gamma) = \frac{\gamma_{\text{K}}^2}{\gamma_{\text{K}}^2 + \gamma^2}$ and γ_{K} is the critical Klein-Nishina Lorentz factor given by

$$\gamma_{\text{K}} \equiv \frac{3\sqrt{5}m_e c^2}{8\pi k_{\text{B}}T} \quad (9)$$

The co-moving energy density of the external photon field is determined in terms of its luminosity and its characteristic radial scale from the SMBH. The dilution of the photon field with the distance of the emission zone is captured by rescaling the energy density with the respective geometric dilution factor $\kappa_{\text{BLR/DT}}^{\text{AGN}}$ (Khangulyan et al. 2014; Acharya et al. 2023) (Described in Appendix B).

At initial time, we inject a total of 10^6 macro-particles that optimally samples the plasma column. Each of these leptonic macro-particles is initialized with a power-law particle distribution $\propto \gamma^{-6}$ with $\gamma_{\text{min}} = 10^2$ and $\gamma_{\text{max}} = 10^8$ for both the simulated jets. The initial number density of electrons within each macro-particle is set to be 2.14×10^{-6} cm $^{-3}$ for the $\Gamma_{c,\text{ini}} = 5$ jet and 8.52×10^{-6} cm $^{-3}$ for the $\Gamma_{c,\text{ini}} = 10$ jet. The initial power-law spectra for these macro-particles are evolved with time, as they propagate within the jet column owing to radiation losses and diffusive acceleration due to shocks. The synchrotron emissivity in the observer's frame is then quantified taking into account the evolving spectra. The emissivity can be further utilized to generate the synthetic synchrotron SEDs directly from the hybrid PLUTO jet simulations using the prescription for νF_ν defined in Dermer & Menon (2009) (see Appendix C).

2.2.1. Diffusive Shock acceleration

PLUTO's hybrid particle module employs analytical estimates for diffusive shock acceleration (DSA) within the test-particle limit, which is valid for highly turbulent relativistic shocks. The module uses a shock detection algorithm to flag shocked regions based on a threshold compression ratio, which is followed by a corresponding change in the post-shock particle distribution associated with each macro-particle.

The changes in the particle distribution due to DSA depends on the compression ratio \mathcal{C} of the shock encountered and the angle φ between the shock normal and the magnetic field vector. The detailed algorithm employed for DSA in the particle module is provided in Vaidya et al. (2018). The compression ratio for the grid cells flagged by the shock detection algorithm is determined as

$$\mathcal{C} = \frac{\beta'_1 \cdot \hat{\mathbf{n}}_s}{\beta'_2 \cdot \hat{\mathbf{n}}_s}, \quad (10)$$

where β'_1 and β'_2 represent the upstream and downstream velocities in the shock rest frame, respectively, while \hat{n}_s is the shock normal vector. The particle distribution $\chi_{LP}^e(\gamma, \tau)$ after the shock, is updated by injecting a power-law spectrum of the electrons in the form,

$$\chi_{LP}^e(\gamma, \tau) = \mathcal{A} \left(\frac{\gamma}{\gamma_{\min}} \right)^{-q+2}, \quad (11)$$

where \mathcal{A} is the normalization factor, γ_{\min} is the lower limit of the normalized particle energy for the electron distribution, and q is the power-law index which is a function of the compression ratio \mathcal{C} .

The updated spectra depend on two free parameters, namely, the non-thermal to thermal number density ratio ζ , and the ratio of total energy of injected particles to fluid internal energy density ζ_E , and also takes into account the old pre-shock particle population. We calculate γ_{\min} and \mathcal{A} by solving

$$\mathcal{A} \int_{\gamma_{\min}}^{\gamma_{\max}} \left(\frac{\gamma}{\gamma_{\min}} \right)^{-q+2} d\gamma = \zeta \frac{\rho}{m} + n^{\text{old}}, \quad (12)$$

$$\mathcal{A} \int_{\gamma_{\min}}^{\gamma_{\max}} \left(\frac{\gamma}{\gamma_{\min}} \right)^{-q+2} \gamma d\gamma = \zeta_E \frac{\mathcal{E}}{m_e c^2} + \frac{E^{\text{old}}}{m_e c^2}. \quad (13)$$

where we interpolate the mass density ρ and the internal energy \mathcal{E} of the fluid at the particle position, while normalized energy upper limit γ_{\max} for the electron distribution is estimated by inserting the following constraints related to particle escape.

In particular, for electrons the first constraint is $\gamma^e \leq \gamma_{\max}^e = eBr_L^{max}/(\beta_{\perp} m_e c^2)$, where the maximum allowed Larmor radius is calculated as $r_L^{max} = r_{LP} \approx 0.5 \min(\Delta x, \Delta y, \Delta z)$ (cell dimensions), where e is the electron charge, B is the magnetic field at the location of the macro-particle and β_{\perp} is the ratio of electron velocity to light speed. For the second constraint, γ_{max} is determined by equating the acceleration and cooling timescales. The minimum of γ_{max} determined through both these conditions is taken as the high energy cutoff for Equations 11, 12 and 13.

2.3. Lepto-hadronic modeling setup

The methodology of our work requires a one-zone lepto-hadronic (OZLH) code that is suitable for modeling radiative processes and neutrino emissions for an individual blazar emission zone. For this purpose, we utilize the code used in Jiménez-Fernández & van Eerten

(2020), which is publicly available at <https://github.com/hveerten/katu>, where it is referred to as *Katu*².

This code solves the kinetic equation for a range of different species of particles which involves leptons (electrons, positrons, muons and anti-muons, electron neutrinos, muon neutrinos and their respective anti-neutrinos) as well as hadrons (protons, neutrons, charged and neutral pions) and photons. The governing kinetic equation is written as,

$$\frac{\partial N(\gamma)}{\partial \tau} = Q_{\text{ex}} + Q_{\text{in}} + \mathcal{L} - \frac{N}{T_{\text{esc}}} - \frac{N}{T_{\text{dec}}} + \frac{\partial}{\partial \gamma} (\dot{\gamma} N), \quad (14)$$

where all the quantities are measured in the co-moving frame unless stated otherwise. Here, $N(\gamma)$ represents the number density distribution for a particular species of particles, the term Q_{ex} accounts for the external injection of particles into the emission region, Q_{in} accounts for the internal injection of the particular particle species created as secondaries inside the region, \mathcal{L} represents particle loss due to internal processes, while N/T_{esc} and N/T_{dec} accounts for the particle loss due to particle escape and decay respectively. Here T_{esc} represents the escape timescale which depends on zone geometry and T_{dec} depicts the decay timescale.

The last term in Equation 14 accommodates the changes due to different radiative emission mechanisms. This term contains $\dot{\gamma}$, accounting for the particle energy losses due to processes such as synchrotron and inverse Compton emission. Here, the radiation energy density adopted for the BLR photon field is done in a similar manner to that of the hybrid particle module (See Section 2.2) and the IC emission is calculated as described in Jiménez-Fernández & van Eerten (2020) using Jones (1968).

The utilized OZLH code can also model electromagnetic processes like Bethe-Heitler (BH) pair production (Kelner & Aharonian 2008), photon-photon pair production (implemented following Boettcher & Schlickeiser 1997), and hadronic processes like photo-meson interaction (Hümmer et al. 2010) along with pion and muon decays which are important processes for astrophysical neutrino production (Lipari et al. 2007; Hümmer et al. 2010).

We want to emphasize that the wide range of processes described above that can be modeled via this code, makes it a useful tool for the modeling of individual emission zones in our framework (see Section 2.4).

² For this study, a few small modifications were made locally to fit the code to our model requirements. Additionally, secondary SED components are generated and stored on a dedicated secondary grid using a local wrapper code

However, we point out that our framework is compatible with any comparable code capable of one-zone leptohadronic modeling, hence to generalize, we will use the acronym OZLH to refer to the usage of such a code for our analysis throughout the text.

2.4. The multi-zone framework

Our multi-zone framework serves as a bridge between the jet dynamics and the micro-physics of the jet. It harnesses the robust dynamical modeling capabilities of the PLUTO code along with its hybrid particle module while building upon the foundation of the single emission zone modeling capabilities of the OZLH code. The flowchart shown in Figure 1 describes the methodology of our work.

We apply the following algorithm to accomplish our objectives:

1. **Dynamical simulation of AGN jet:** We start by simulating the dynamics of a relativistically moving magnetized section of an AGN jet using PLUTO code, and incorporate electron macroparticles which advects with the flow. We provide a perturbation to the radial velocity of the jet and evolve it until current-driven instabilities set in.
2. **Optimal time selection:** Based on the evolution of various energy components within the jet, we select an optimal time for conducting our multi-zone analysis. This time corresponds to an intermediate point during the linear growth phase of the kink instability formation process in the jet. This phase is particularly suitable, as it generates complex magnetic field configurations facilitating a dynamic interplay between particle acceleration and cooling mechanisms, while also ensuring that cooling is not yet dominant on the system.
3. **Multi-zone division:** At the selected dynamical time, we segment the jet into multiple spherical emission zones, with the zone radius decided by the local radius of the jet at the position of the emission zone.
4. **Calculating zone parameters:** For each zone we compute the fluid parameter averages and net electron distribution³ parameters using the jet simulation data. Since the particle module used in the jet simulations does not provide us with a

proton distribution, we rely on approximations to estimate it. (Detailed discussion in Section 2.4.1).

5. **Bridging jet dynamics and microphysics:** The average fluid and particle distribution parameters, calculated for each zone from the jet simulation in the previous step, are provided as input parameters to our multi-zone leptohadronic framework, which is modeled and executed using an OZLH code. Leveraging fluid simulations to inform emission zone modeling parameters significantly narrows the dimensions of the multi-zone parameter space.
6. **Zonal simulations:** We use the OZLH code used for Jiménez-Fernández & van Eerten (2020) to perform steady-state leptohadronic simulations for individual zones by incorporating the relevant leptonic and hadronic processes. This provides us with the photon and neutrino emissions from each zone.
7. **Multi-zone SED generation:** We stack the emissions that are contributed by each zone to generate the multi-zone photon SED and neutrino flux.

2.4.1. Initial parameters and approximations for the multi-zone framework

Most OZLH codes including the one we use do not incorporate the fluid dynamical evolution of the jet. However, connecting such a code with 3D RMHD simulations via our multi-zone framework, provides us with an ideal platform for simulating blazar emissions. We may therefore model emissions from individual zones of the jet stream by using the OZLH code, following the algorithm we have described above.

We perform a leptohadronic analysis, for the RMHD jet column simulations having $\Gamma_{c,ini} = 5$ and 10 at the dynamical times $t = t_{s1} = 782$ years and $t = t_{s2} = 743$ years, respectively. These times align with the initial phase of the instability formation process (see detailed discussion in Section 3.1).

At times t_{s1} and t_{s2} , we divide the respective jet columns into six distinct, spherical emission zones. The zones are distributed along the jet axis, denoted by the numbers 1 to 6 from the bottom to the top of the column, respectively. We hereby assume the individual zones in our multi-zone framework to be independent emission regions.

For each zone, we model the synchrotron emission from both leptons and hadrons, synchrotron self-Compton (SSC) emissions, B-H pair production, photon-photon ($\gamma\gamma$) pair production and photo-meson

³ Throughout the text, the terms *electron distribution*, *proton distribution*, or *particle distribution* refer to the distribution of the respective particle species' number density over an energy range.

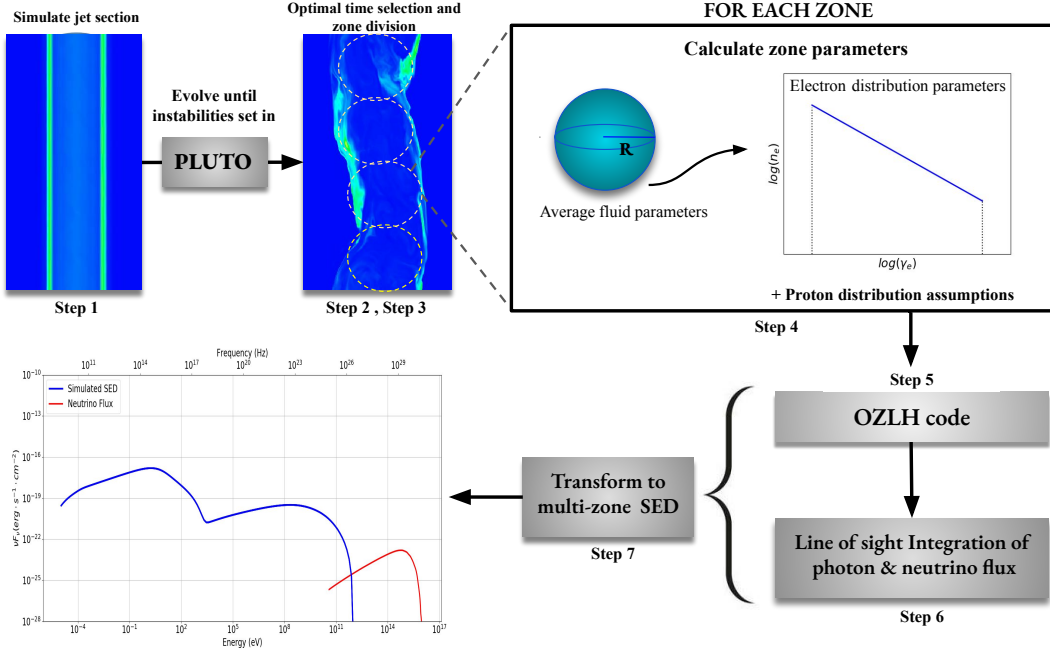


Figure 1. Flowchart depicting the methodology used in our lepto-hadronic multi-zone framework. The step numbers directly correspond to the order of steps for the algorithm as described for the framework in the paper text.

interaction. Each zone hosts $\approx 10^4 - 10^5$ macro-particles. The normalized spectra for leptons, χ_{LP} , for each macro-particle is defined via Equation 5 and evolved following Equation 6. This evolution does not explicitly account for energy losses due to SSC to avoid high computational cost of implementing SSC losses in our dynamical runs.

Further, in the majority of the zones, synchrotron cooling timescales are much shorter than SSC cooling timescales. Therefore, in these zones the final electron distributions will be primarily governed by synchrotron losses. However, we observe that in one or two zones SSC cooling may become important. In such cases, not accounting for SSC cooling, overestimates the number density of high energy electrons, and consequently the photon flux from these zones in certain frequency bands. As a consequence, this can impact the photon field available for the photo-meson process, and hence the neutrino fluxes that are estimated for these zones may constitute an upper limit only.

In summary, there are a total of 11 initial parameters required for the steady-state lepto-hadronic modeling for each zone. By these parameters we are able to connect the emission zone modeling with the OZLH code to the dynamics of the RMHD simulations. In our approach,

these zonal input parameters⁴ for a selected dynamical time are determined as follows:

- **Non-thermal density, $\rho_{\text{zone}}^{\text{NT}}$:** Derived from the spatially averaged fluid density in each zone of the jet simulations,

$$\rho_{\text{zone}}^{\text{NT}} = \left(\frac{\zeta}{1 + \zeta} \right) \langle \rho \rangle_{\text{zone}} \quad (15)$$

where ζ represents the ratio of non-thermal density to the thermal density in the zone. This is a free-parameter which we choose to be 0.15 for all zones across the jet.

- **Proton to electron number density ratio (η_{zone}):** The ratio given by $\eta_{\text{zone}} = n_{\text{zone}}^{\text{p}}/n_{\text{zone}}^{\text{e}}$, is constrained by ρ^{NT} and ζ for each zone in the jet as specified below:

$$\rho_{\text{zone}}^{\text{NT}} = \frac{\zeta}{1 + \zeta} \langle \rho \rangle_{\text{zone}} = n_{\text{zone}}^{\text{e}} (m_e + \eta_{\text{zone}} m_p) \quad (16)$$

where m_e and m_p are electron and proton mass, $n_{\text{zone}}^{\text{e}}$ and $n_{\text{zone}}^{\text{p}}$ are electron and proton number densities within the zone respectively.

⁴ All input parameters labeled with the subscript “zone” are zone-dependent, i.e., they may take on different values for each emission zone.

- **Magnetic field** (B_{zone}): Determined from the average co-moving magnetic field in each zone of the jet simulations.
- **Zone radius** (R_{zone}): The radius of the spherical zones, R_{zone} , is derived from the average radius of the jet cross-section, $R_{\text{jet}}(z_c)$, at $z = z_c$, the location of the center of the spherical zone along the z -axis. Hence, the number of zones we take for our multi-zone modeling is dependent on the radius of the jet at the chosen time.
- **Doppler factor** (δ_{zone}): The Doppler factor for each grid cell of the 3D jet simulation is calculated as follows:

$$\delta_{\text{cell}} = \frac{1}{\Gamma_{\text{cell}}(1 - \beta_{\text{cell}} \cdot \hat{\mathbf{s}})} \quad (17)$$

where Γ_{cell} is the bulk Lorentz factor for the grid cell while β_{cell} represents the grid cell velocity normalized to light speed, $\hat{\mathbf{s}}$ is the unit vector for the line of sight. We then average over all the grid cells within the zone to obtain δ_{zone} ,

$$\delta_{\text{zone}} = \frac{\int_{\text{zone}} \mathcal{T} \delta_{\text{cell}} dV}{\int_{\text{zone}} \mathcal{T} dV} \quad (18)$$

where \mathcal{T} is the tracer variable, dV is the co-moving volume of the cell.

- **Electron distribution** - ($\alpha^e, \gamma_{\text{min}}^e, \gamma_{\text{max}}^e$): The electron distributions from all the macro-particles within a particular zone of the jet are used to estimate the net electron distribution for the zone as follows:

$$N_{\text{net}}^e(\gamma) = \sum_i n_{F,i} \chi_{\text{LP},i}^e(\gamma) \quad (19)$$

where $N_{\text{net}}^e(\gamma)$ represents the net number density function for the electron distribution within an emission zone defined over the energy range $[\gamma_{\text{min}}^e, \gamma_{\text{max}}^e]$, $n_{F,i}$ is the fluid number density at the location of the i^{th} Lagrangian particle in the zone, $\chi_{\text{LP},i}^e$ is the normalized number density distribution for the i^{th} Lagrangian particle. Here, we calculate $\gamma_{\text{min}}^e = \min(\{\gamma_{\text{min},i}^e\}_{\text{zone}})$ and $\gamma_{\text{max}}^e = \max(\{\gamma_{\text{max},i}^e\}_{\text{zone}})$, where $\{\gamma_{\text{min},i}^e\}_{\text{zone}}$ and $\{\gamma_{\text{max},i}^e\}_{\text{zone}}$ denotes the sets of minimum and maximum γ for each Lagrangian particle in the zone.

Depending on the zonal net distribution of electrons, we fit N_{net}^e with either a *power-law* (PL) or a *power-law with an exponential cutoff* (PLEC)

and get the required electron distribution parameters:

$$\begin{aligned} N_{\text{fit,PL}}^e &= A_{\text{fit}}^e \gamma^{-\alpha_{\text{fit}}^e} \\ N_{\text{fit,PLEC}}^e &= A_{\text{fit}}^e \gamma^{-\alpha_{\text{fit}}^e} e^{(-\gamma/\gamma_{\text{break}}^e)} \end{aligned} \quad (20)$$

where A_{fit}^e is the normalization factor for the fitted curve to the electron distribution which can either be PL or PLEC depending on the zone, α_{fit}^e is the power-law index for the fitted curve and γ_{break}^e represents the energy for the exponential cutoff for the PLEC fitted curve. From this we can get the input parameters for electron distribution like $\alpha^e = \alpha_{\text{fit}}^e$ while the γ_{min}^e and γ_{max}^e remains the same for the fitted curve and the net distribution within the zone.

- **Proton distribution** - ($\alpha^p, \gamma_{\text{min}}^p, \gamma_{\text{max}}^p$): Since the jet simulations with the hybrid particle module does not provide us with a proton distribution, we have taken 4 cases of assumptions for the proton distribution parameters for each zone as depicted in table 1.

By using the initial parameters determined from our jet simulations at the chosen optimal times t_{s1} and t_{s2} , respectively, the lepto-hadronic analysis parameters for each zone can be derived as detailed above. For each jet simulation, Table 2 reports the range of these zonal parameters, from the minimum to the maximum of the parameter values across the six zones.

In our model the temporal evolution of the primary electron population is computed with the dynamical evolution of the jet, accounting for the different acceleration and cooling processes using the particle module in PLUTO. Note that this approach also helps us draw inference for the primary proton distribution (see below).

For the lepto-hadronic analysis however, we adopt a hybrid/quasi steady-state model where the initial primary electron and proton populations are assumed to have settled in a steady state. This can be interpreted as a scenario where the underlying dynamics and associated acceleration processes do continuously inject non-thermal particles in each zone, which maintain the primary particle distribution (given to us by the hybrid RMHD simulation) for the duration of the lepto-hadronic analysis (i.e for the time needed for the solution of the time-dependent kinetic equations to reach a steady state, thus $T_{\text{stop}} = T_{\text{ss}}$).

Table 1. Model assumptions for the proton distribution.

	Case 1	Case 2	Case 3	Case 4
Distribution type $N^p(\gamma)$	$\eta_{\text{zone}} N_{\text{fit}}^e(\gamma)$	$\eta_{\text{zone}} N_{\text{fit,PL}}^e(\gamma)$	$\eta_{\text{zone}} N_{\text{fit,PL}}^e(\gamma)$	$\eta_{\text{zone}} N_{\text{fit,PL}}^e(\gamma)$
α^p	α_{fit}^e	α_{fit}^e	α_{fit}^e	2.0
γ_{max}^p	γ_{max}^e	γ_{max}^e	Constrained by Hillas criterion	γ_{max}^e

NOTE— These parameters are used as input for the OZLH code, based on the fitted electron distributions from PLUTO simulations. In Case 1, $N_{\text{fit}}^e(\gamma)$ can have either a *power-law* (PL) or *power-law with exponential cutoff* (PLEC) form, depending on the zone. Case 3 applies the Hillas condition to constrain γ_{max}^p .

Table 2. Input parameters for the lepto-hadronic multi-zone modeling.

Jet	$\rho_{\text{zone}}^{\text{NT}}$ (10^{-26} g cm $^{-3}$)	η_{zone} (10^{-2})	B_{zone} (10^{-2} G)	R_{zone} (10^{18} cm)	δ_{zone}	α_{fit}^e	γ_{min}^e	γ_{max}^e (10^6)
$\Gamma_{\text{c,ini}} = 5$	2.7 – 4.9	0.42 – 1.01	1.69 – 2.14	6.172	1.78 – 2.77	2.65 – 3.10	14.76 – 23.24	49.66 – 205.15
$\Gamma_{\text{c,ini}} = 10$	1.34 – 5.41	0.07 – 1.34	1.83 – 3.15	6.172	1.95 – 3.54	2.47 – 3.17	8.21 – 14.65	8.64 – 333.41

NOTE— The values show the range (minimum to maximum) across the six zones at the selected dynamical times (t_{s1} and t_{s2}) when the multi-zone analysis is done for each jet simulation.

Our hybrid-particle module that is coupled to the fluid dynamics, applied to derive the evolving electron spectra, should be understood as a pilot study that is able to bridge the complex jet dynamics with associated shocks and fluid instabilities that is required to shape realistic electron spectra. Our approach is in contrast to existing emission zone modeling which assumes a fixed power-law particle injection (as e.g. adopted in Xue et al. (2019)) throughout the evolution. Since, we are essentially estimating the neutrino and photon flux by post processing from an MHD simulation snapshot, we are inherently assuming that the primary electron distribution obtained from our hybrid model does not substantially evolve within one dynamical time step.

The spectra of the other particle species that are generated as secondaries are evolved with time by solving their respective kinetic equations until a 'final' steady state condition is achieved - marked by both the photon, and neutrino populations simultaneously satisfying the following steady state saturation criteria,

$$\sqrt{\int \left[\frac{1}{N^i(\gamma)} \frac{\partial N^i(\gamma)}{\partial t} \right]^2 d\gamma} < 10^{-8} \quad (21)$$

where, $N^i(\gamma)$ represents the number density at energy γ of a particle species 'i'. This criterion is the L^2 -norm of the fractional time derivative of $N^i(\gamma)$, i.e. it quantifies the relative rate of change of the particle population with respect to time for each particle species.

The SED is evaluated only after both the photon and neutrino components have reached steady-state, because the SED depends directly on their steady-state populations and additionally neutrinos are among the last particle species to form.

There are three important timescales that are relevant for our analysis, which are (i) the time needed for the system to achieve the 'final' steady state in our lepto-hadronic framework, T_{ss} , (ii) the light crossing/escape time $\sim R_b/c$, and (iii) the dynamical timescale of the jet $T_{\text{dyn}} \sim R_b / \langle v_{\text{fluid}} \rangle$. We have seen that for our specific simulations for each zone $T_{\text{ss}} \sim R_b/c$, which is much smaller than T_{dyn} for the chosen jet snapshot used for the lepto-hadronic analysis.

Further, since the snapshots of the jet from the RMHD simulations are taken at times $t_s \gg R_b/c$, we can safely assume that the particle distribution has already achieved steady-state by then. Thus, we may hold, under this approximation, the primary electron and pro-

ton populations fixed during the window of our lepto-hadronic analysis within $[t_s, t_s + T_{ss}]$ and evolve only the secondary species to steady state. This is justified because the fluid dynamics that is governing the Lagrangian particle distributions, evolves appreciably only over the larger dynamical timescale T_{dyn} .

In summary, we initially prescribe a primary electron and proton population, with the number density of all secondary particle species set to zero. The secondary species populations are then progressively built up till the 'final' steady state condition is satisfied.

As briefly mentioned earlier, PLUTO's hybrid particle module only has provisions to incorporate electrons so far, we therefore adopt heuristic approximations for the proton distribution parameters based on the electron distribution parameters of each zone. This is based on the idea that the evolved electron distribution at the selected dynamical times $t = t_{s1}$ and t_{s2} for the respective jets, carries information about the history of acceleration and cooling processes the region has undergone during the dynamical evolution of the jet.

For Case 1, we assume that the proton distribution has a similar functional form to the electron distribution obtained from the fitted spectra which can either be PL or PLEC. In Case 2, we take into consideration the fact that when compared to electrons, synchrotron and inverse Compton cooling is significantly less efficient for protons because of higher proton mass, resulting in much longer cooling timescales in protons. Hence, in this case we assume a simple power-law for protons but with no exponential cut-off for cooling. Additionally, we assume the proton distribution to have the same slope (in log scale) as the power-law portion of the fitted spectra for the electron distribution in each zone. Case 3 is similar to case 2 but we determine the γ_{max} of the proton distribution using the Hillas criterion which constraints the maximum allowed Larmor radius of the protons using the size of the emission zone. For Case 4, all other parameters are similar to Case 2 but this time we choose a much flatter power-law index ($\alpha^p = 2.0$).

In all four cases, we assume the normalization constant of the proton distribution, A^p , is scaled by the zonal proton-to-electron number density ratio (η_{zone}), as compared to the electron distribution. The proton distribution normalization constant is defined as follows:

$$A^p = \eta_{\text{zone}} A_{\text{fit}}^e. \quad (22)$$

This ensures consistency with the proton number density considered for the zone, based on the η_{zone} constraint described earlier.

2.4.2. Multi-zone SED modeling

Following the steps specified in our multi-zone framework algorithm and utilizing the initial parameters as described in Section 2.4.1 for the framework, we get a resultant photon and neutrino distribution when the steady state convergence criteria (Equation 21) is satisfied for individual zones. These photon and neutrino distributions can be used to generate the observed photon SED and neutrino flux for each zone i.e. the "zonal SEDs" using the following expression (Dermer & Menon 2009; Böttcher & Baring 2019; Jiménez-Fernández & van Eerten 2020),

$$\nu F_\nu = \epsilon'^2 N'_{\text{ph}}(\epsilon') m_e c^2 \frac{\delta_{\text{zone}}^4}{4\pi(1+z)d_L^2} \frac{V'}{T'_{\text{esc}}} \quad (23)$$

For this equation, to illustrate the transformation between the co-moving and observer frames, we use primed quantities for the co-moving frame and un-primed quantities for the observer frame⁵. Here, ϵ' is the photon energy, normalized to the rest mass energy of an electron, $N'_{\text{ph}}(\epsilon')$ is the photon population density as a function of energy ϵ' , $m_e c^2$ is the rest mass energy of an electron, z is the redshift of the source, d_L is the luminosity distance of the source, V' is the volume of the emission region, and T'_{esc} is the escape timescale for photons. A similar approach is applied to neutrinos, adopting the standard consideration that they arrive at Earth in a 1 : 1 : 1 flavor ratio (Aartsen et al. 2015). This leads us to the final step of the algorithm where we combine the simulated emissions contributed by each zone by stacking the zonal SEDs. This process generates the desired lepto-hadronic multi-zone SED consisting of both multi-wavelength and neutrino fluxes for a section of the blazar jet.

3. FROM DYNAMICS TO SYNTHETIC EMISSION SIGNATURES

In this study, we have performed a detailed analysis of morphologically intriguing regions that arise from the interdependence between instabilities and shock structures in the AGN jet simulations. We begin by presenting results from our non-resistive 3D RMHD simulations, which model cylindrical, relativistic, and magnetized section of an AGN jet. This is followed by a zonal analysis of the different regions of interest. We then present findings from our lepto-hadronic multi-zone analysis using the algorithm described in Section 2.4, that yields photon and neutrino SEDs which offer fun-

⁵ Previously, we refrained from using primed notation for the sake of convenience, as most quantities were defined in the co-moving frame.

damental insights into the internal dynamics of the jet and its correlation with emission signatures.

3.1. Dynamical evolution

We have simulated cylindrical sections of parsec-scale jets with two different bulk Lorentz factors, $\Gamma_{c,\text{ini}} = 5$ and 10 along the jet axis. The jets are initialized with a rotational velocity profile along with both poloidal and toroidal magnetic field components. A detailed description of the initial parameters and boundary conditions for the jet simulations is provided in Section 2.1 and Appendix A.

The relativistic and magnetized jet simulations presented here are particularly susceptible to current-driven instabilities due to the presence of a prominent toroidal magnetic field along with a radial velocity perturbation of the form described in Equation (3). Such a perturbation incorporates sausage, kink and fluting modes of instabilities, each competing for dominance. It also subsumes waves of different frequencies as well as randomized phase shifts. Therefore, proving to be well-suited for simulating realistic conditions where the jet maybe subjected to a variety of disturbances which may stem from sources like disk winds, jet precession, etc.

In our work, we primarily observe the emergence of a helical instability as the jet simulations evolve with time for both $\Gamma_{c,\text{ini}} = 5$ and 10 jets. A good diagnostic tool to differentiate whether the helical displacement is dominated by the current-driven kink instability, or the Kelvin-Helmholtz instability, is the Alfvén Mach number \mathcal{M}_A , which can be defined as (Bodo et al. 2019),

$$\mathcal{M}_A = \frac{\Gamma_c^2(1 - v_A^2)}{v_A^2}. \quad (24)$$

Here, \mathcal{M}_A essentially gives the ratio between matter energy density and magnetic energy density, $v_A = B/\sqrt{\rho h + B^2}$ is the Alfvén speed (for $c = 1$), and h is the specific enthalpy. Both jets start out with an average Alfvén Mach number of unity, but quickly transition to a sub-Alfvénic flow. The onset of the helical instability, coincides with a rise in \mathcal{M}_A , consistent with a decline in magnetic energy and a rise in transverse (xy -plane) kinetic energy density.

Despite the increase in \mathcal{M}_A during the growth of the kink instability, the $\Gamma_{c,\text{ini}} = 5$ jet still remains sub-Alfvénic throughout the simulation time, while the $\Gamma_{c,\text{ini}} = 10$ jet transitions from sub-Alfvénic during the instability formation process to marginally trans-Alfvénic in the later stages of the simulation. This is most probably due to faster hydrodynamic evolution (larger Lorentz factor) in the latter, as both jets exhibit similar magnetic field strengths during the later stages.

These trends suggest that the helical deformations in both jets are primarily due to current-driven kink instabilities, owing to their predominantly sub-Alfvénic flow. However, the faster jet begins to exhibit some shear-driven features in the later stages, possibly indicating a minor contribution from Kelvin-Helmholtz instability dynamics as the jet velocity approaches the Alfvén speed.

In Figure 2, we present the temporal evolution of the density, thermal pressure, and magnetic pressure for the $\Gamma_{c,\text{ini}} = 5$ jet. The kink instability, characterized by a non-axisymmetric helical displacement of the jet body, grows when the magnetic pressure locally exceeds the stabilizing effect of magnetic tension.

With the onset of the kink mode in Figure 2, we observe that regions of elevated density correlate with enhancements in thermal pressure. We interpret this as indicative of shock formation, which is marked by discontinuities in density, pressure and also the local flow speed. Notably, these regions also correspond to amplified magnetic pressure. Since we operate in the non-resistive, ideal MHD regime in our relativistic simulations, matter is expected to be more concentrated in such regions, simply due to flux-freezing.

Kink-induced distortions can trigger the formation of multiple shocks and regions of intense magnetic compression, which in a resistive MHD scenario could serve as ideal sites for magnetic reconnection (Striani et al. 2016; Medina-Torrejón et al. 2021). As evident from the figure, while such regions are present across the jet, they are more concentrated near the sites where prominent helical displacements occur, consequently triggered by the formation of a jet kink. We observe a qualitatively similar morphological evolution for the $\Gamma_{c,\text{ini}} = 10$ jet, which for brevity we omit from the main text of the paper.

In Figure 3 we illustrate how the formation of the instability plays a significant role in governing the evolution of the different energy components of the jet over time. We have calculated the volume-averaged components of energy density for the jet in the lab frame (see Equation 10 in Dubey et al. 2023). The formation of the kink instability advances through linear and non-linear phases. In the linear phase, small perturbations to the equilibrium state of the plasma grow over time resulting in the formation of a helical kink instability, marked by a rise in the transverse(xy -plane) kinetic energy of the jet. The system transitions into the non-linear phase as the transverse kinetic energy declines, characterized by a significant transverse deformation of the overall jet structure. Simulation studies such as Mizuno et al. (2009, 2011, 2012); O’Neill et al. (2012); Acharya et al.

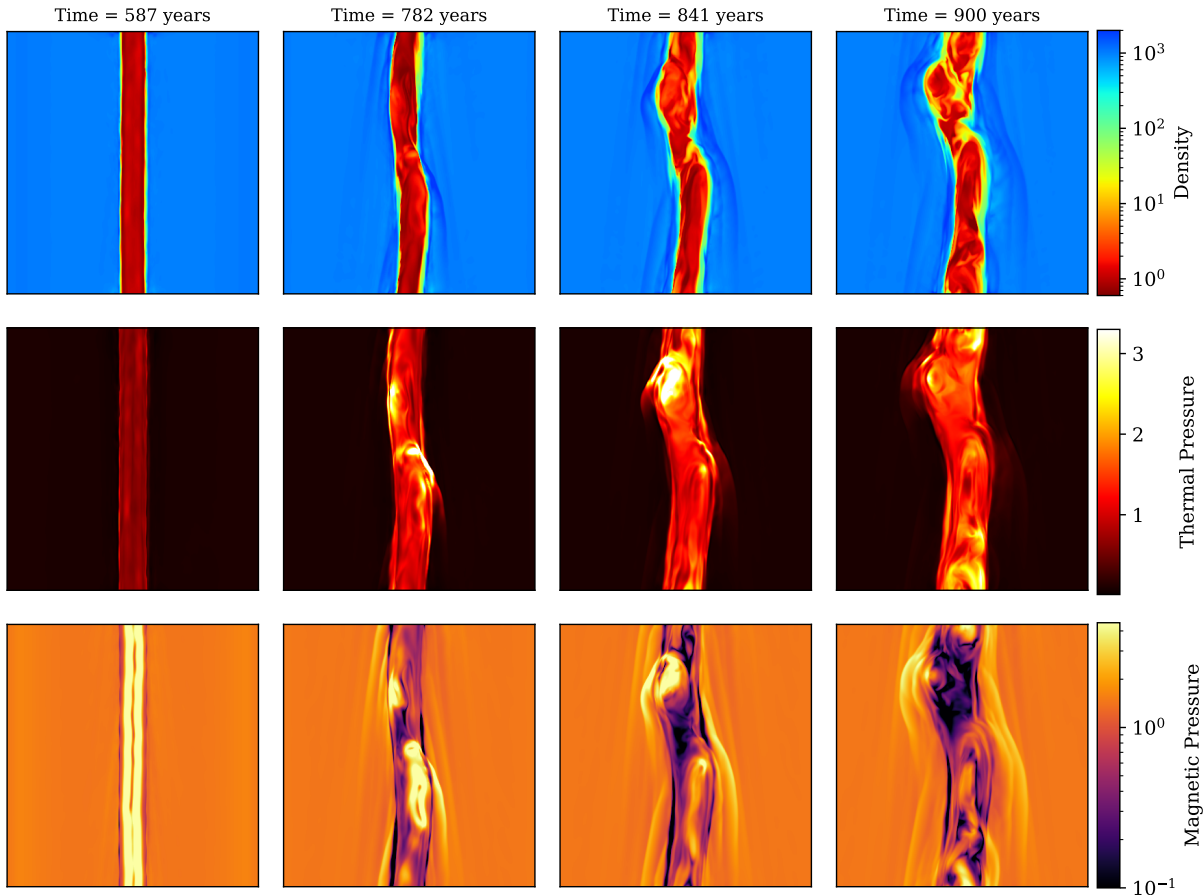


Figure 2. Magneto-hydrodynamic evolution of the jet. Shown are yz -plane slices for the density (top), thermal pressure (middle) and magnetic pressure (bottom) at several simulation times for the jet with $\Gamma_{c,ini} = 5$. All quantities are in code units.

(2021) give significant insights on these phases of kink instability growth.

During the linear growth phase, the perturbation causes a reconfiguration of the initially ordered toroidal magnetic field within the jet, causing spatial variations in the field strength across the jet. This introduces imbalances in magnetic tension which drives the plasma into a helical displacement pattern. The growing instability causes the magnetic energy of the jet to decline as the field distorts further from its initial configuration, weakening the toroidal component locally. The associated transverse motion of the plasma during the development of the kink leads to an increase in transverse kinetic energy. To highlight the linear phase for each jet, we have shaded the corresponding region gray in Figure 3.

A portion of the magnetic energy lost by the jet during kink formation, is fed into the transverse kinetic energy channel and the thermal energy of the jet, while the remaining part is lost to the ambient medium surrounding the jet. We suggest that this possibly happens due to the shocks produced in the ambient medium due to a

combination of kink induced deformations (see Figure 2) and jet rotation.

Figure 4 presents 3D visualizations of the magnetic field lines at the chosen simulation times for each jet. The structure of the magnetic field lines clearly illustrates how the bending of the toroidal field component distorts the body of the jet, leading to kink formation. We see that there exists a higher concentration of magnetic field lines at the location of the kink distortions, which is also reflected in the respective density, thermal pressure, and magnetic pressure distribution.

In this work, we are interested in exploring whether intrinsic shocks produced during the linear growth phase of the kink instability, can generate significant neutrino emissions. As the jet progresses into the later stages of kink evolution, we see that the particle spectra across the zones show significant exponential cooling. Hence we select a simulation time near the midpoint of the linear phase to perform the multi-zone analysis (black dashed lines in Fig. 3). This allows us to study the interplay of both shock-driven particle acceleration as well

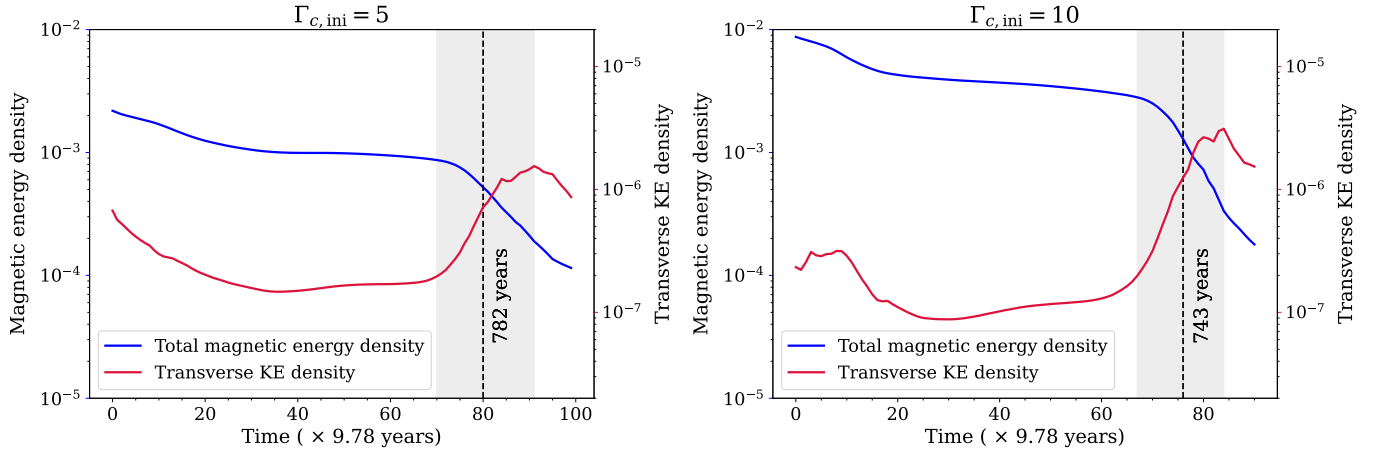


Figure 3. Evolution of total magnetic energy density and the transverse (xy -plane) kinetic energy density for the jets with $\Gamma_{c,ini} = 5$ (left panel) and $\Gamma_{c,ini} = 10$ (right panel), respectively. The linear phase of kink instability formation is shaded gray and the dashed black line represents the optimal time slice chosen for the multi-zone analysis ($t_{s1} = 782$ years for the $\Gamma_{c,ini} = 5$ jet and $t_{s2} = 743$ years for the $\Gamma_{c,ini} = 10$ jet). There are two vertical axes in each plot, the total magnetic energy density (blue solid line) is associated with the vertical axis on the left side of the plots while the vertical axis on the right side is associated with the transverse kinetic energy density (red solid line) for each plot.

as radiative cooling without the latter suppressing the imprints of shock acceleration on the particle spectra.

3.2. Zonal analysis

In Figure 5, we show the thermal pressure for the selected time instance $t_{s1} = 782$ years for $\Gamma_{c,ini} = 5$. The thermal pressure for both yz and xz -slices of the jet have been presented to illustrate the rationale behind the zone selection. As evident from the figure, we have segregated the jet column into six spherical zones. The centers of the spherical zones have been strategically positioned, such that the spheres encompass regions of elevated pressure which serve as signatures of shocks, generated due to the structural deformities caused by the formation of kink instability. Regions with a higher concentration of shocks are located near the kinks due to the pronounced deformation of magnetic field lines in those regions. This results in abrupt changes in plasma parameters, such as density, pressure and velocity leading to the formation of localized areas with increased shock activity.

Subsequently, we present the electron distribution for all six zones for the jet with $\Gamma_{c,ini} = 5$ in Figure 6. The electron distribution reveals that regions with elevated pressure are associated with a flatter electron power-law distribution. Additionally, these regions also exhibit an exponential cutoff in their power-law spectra. This possibly arises from heightened radiative cooling activity induced by mechanisms like synchrotron and inverse Compton cooling in regions containing intense shocks and enhanced magnetic field variations.

For the jet with $\Gamma_{c,ini} = 5$, in Figure 5 we can see that Zone 4 stands out among all the zones, as it encloses one of the helical kinks along with the largest high pressure region in the jet possibly arising due to shock induced plasma compression. Consequently, the electron distribution for this zone as depicted in Figure 6, shows the flattest power-law spectrum in the jet with an index of $\alpha_{fit}^e = 2.65$.

To understand how the shock strength associated with these dynamical signatures influences particle acceleration, in Figure 7 (top panel) we present a histogram for the compression ratio of the last encountered shock for the electron Lagrangian particles within the six spherical zones of the $\Gamma_{c,ini} = 5$ jet. We see that Zone 4, which features both a helical kink and a very prominent high-pressure region, consistently shows a higher number of macro-particles that have traversed through shocks with larger compression ratios. This suggests that such regions act as hotspots for the formation of strong shocks. Motivated by these results, we plot a step histogram (bottom panel of Figure 7) for the γ_{max} of each Lagrangian particle within Zone 1 and Zone 4 - representing the zones with the lowest and highest number of Lagrangian particles undergoing high-compression-ratio shocks, respectively. We observe that Zone 4 indeed has more particles getting accelerated to higher energies compared to Zone 1, as the latter lacks a prominent high pressure region and has a much steeper electron distribution (see Figure 6).

Figure 8 illustrates the thermal pressure for the selected time instance $t_{s2} = 743$ years for the $\Gamma_{c,ini} = 10$ jet. Here again we have divided the jet into six spheri-

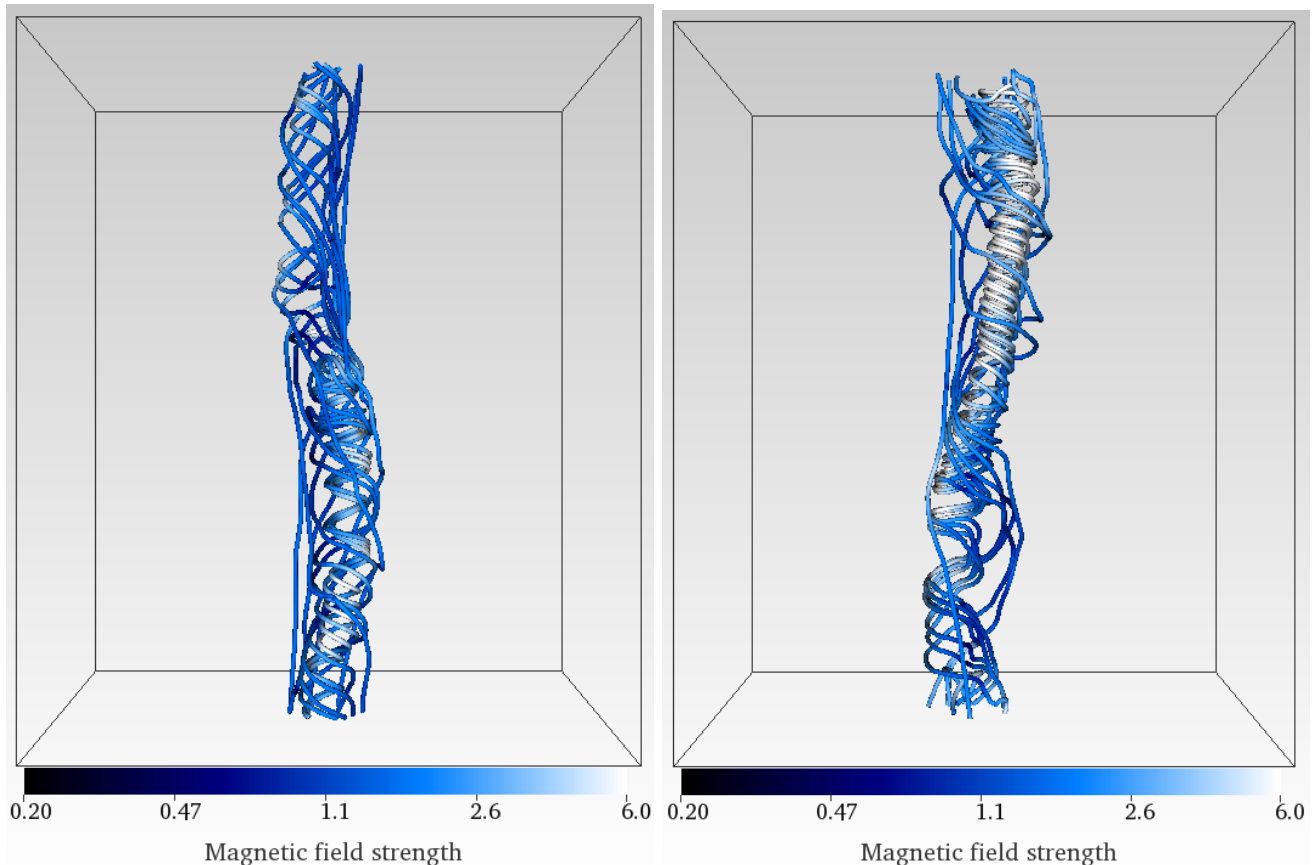


Figure 4. Magnetic field structure for the two jet simulations with different initial jet speed. Shown are the field lines for the jet with $\Gamma_{c,ini} = 5.0$ at $t_{s1} = 782$ years (*left panel*) and for the jet with $\Gamma_{c,ini} = 10.0$ at $t_{s2} = 743$ years (*right panel*). The color bar represents the magnetic field strength (in code units).

cal zones. As evident from the figure, we observe that Zones 1, 3 and 6 in the yz -plane show indications of high pressure regions which are characteristic signatures of shocks. The jet column also shows bending at these locations which is consistent with the $\Gamma_{c,ini} = 5$ jet simulations. While in the xz -plane the shock signatures are observed in Zones 1 and 6.

Figure 9 depicts the respective electron distributions for all six zones of the $\Gamma_{c,ini} = 10$ jet. A pattern similar to the zonal analysis of the $\Gamma_{c,ini} = 5$ jet, can be observed for the $\Gamma_{c,ini} = 10$ jet simulation, where Zone 6 consisting of the highest pressure region, corresponds to the flattest electron power-law distribution with an index of $\alpha_{fit}^e = 2.47$.

These results indicate that varying particle distributions emerge from different emission zones, as the jet undergoes instability dynamics. Additionally, higher pressure regions are associated with flatter particle distributions, likely due to heightened shock dynamics resulting in more efficient acceleration processes. Additionally, such regions exhibit exponential cooling in higher energies, potentially arising from amplified radiative cooling

that modifies the underlying electron energy distribution in those zones.

3.3. Multi-zone SED

We present the multi-zone SEDs for all four proton distribution cases considered (see Table 1) for the two jet simulations in Figure 10. These SEDs are obtained by combining the line-of-sight integrated contributions from individual zonal SEDs across the six emission zones. In this figure, we depict both the multi-wavelength photon flux as well as the combined muon neutrino and anti-neutrino ($\nu_\mu + \bar{\nu}_\mu$) flux in the observer frame. This has been calculated as one-third of the total neutrino population generated at the source to take into account neutrino oscillations. For the SED modeling, we have assumed a redshift of $z = 0.3365$, identical to the TXS 0506+056 source, which gives us a luminosity distance of $d_L = 1762$ Mpc. Additionally, we assume the jet to be a blazar, with the jet axis making an angle of $\theta_{los} = 1^\circ$ with our line of sight.

For both jet simulations, we find that a clear trend emerges for the neutrino flux for the four proton dis-

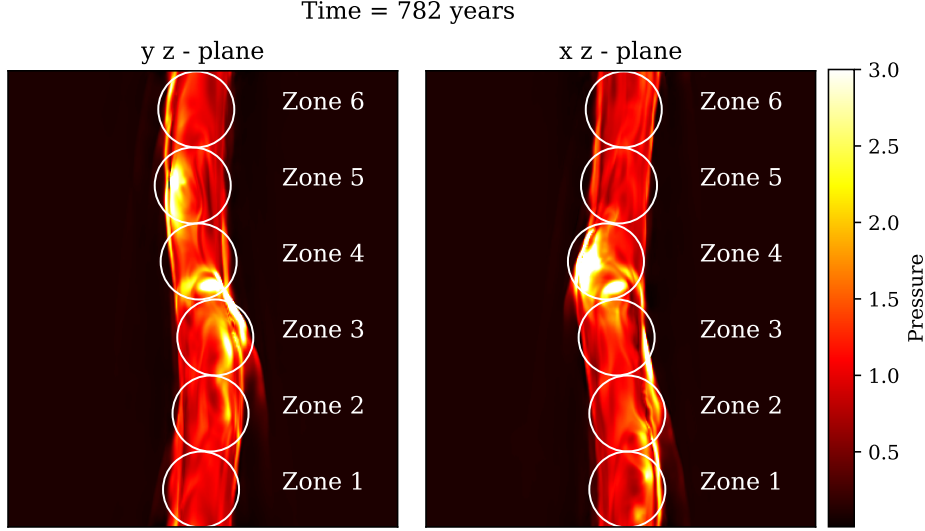


Figure 5. Slices of the yz -plane (*Left*) and the xz -plane (*Right*) with their color representing the thermal pressure (see color bar) for the jet with $\Gamma_{c,ini} = 5.0$ at time $t_{s1} = 782$ years. The respective spherical zones are marked by white circles.

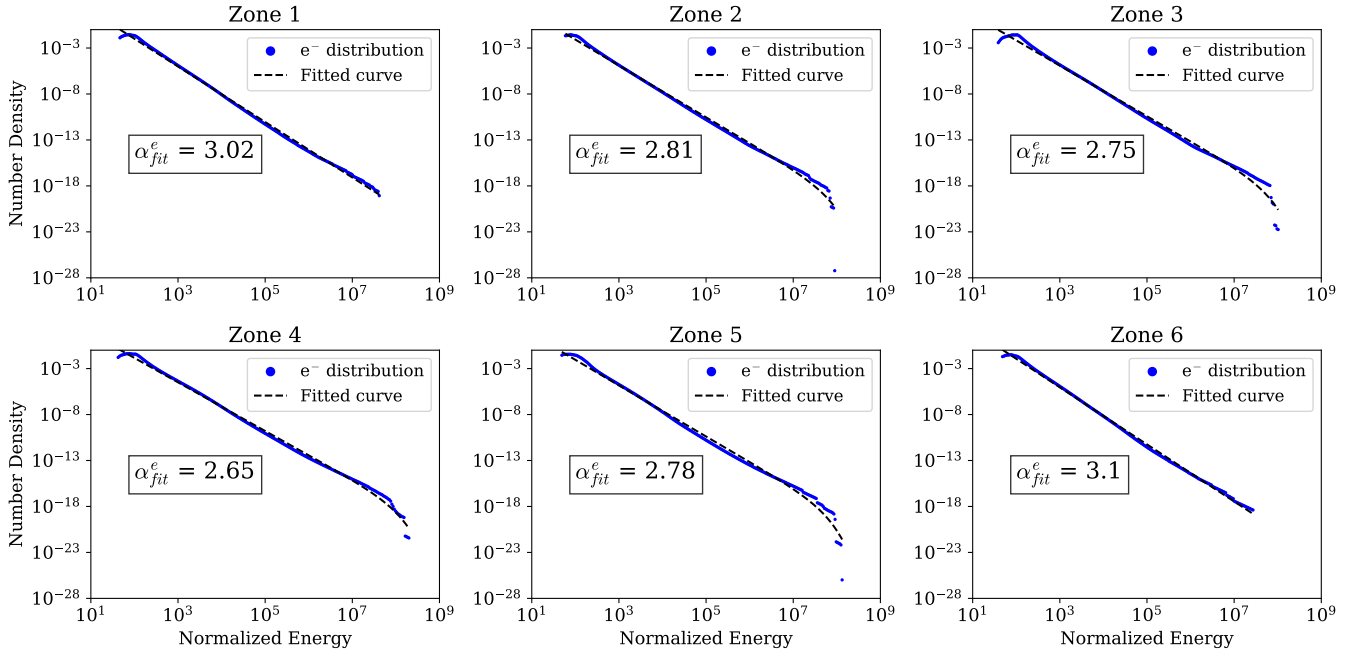


Figure 6. The respective electron distributions and the fitted PL/PLEC curve for the six zones of the jet with $\Gamma_{c,ini} = 5$ at time $t_{s1} = 782$ years.

tribution cases. Compared to Case 1, we observe an increase in the multi-zone neutrino flux for both jets in Case 2. The Case 3 setup not only exhibits a noticeable enhancement in neutrino flux, but also displays flux distributed over a broader energy range, due to more higher energy protons being available to participate in the photo-meson interaction owing to the Hillas criteria. For Case 4, we see a significant increase in the neutrino

flux compared to the other cases, which arises from the power-law of the proton distribution being assumed to be very flat with an index of $\alpha^P = 2.0$. We also observe that the flux for both photon and neutrino flux is a few orders of magnitude higher for the jet with $\Gamma_{c,ini} = 10$, as compared to the jet with $\Gamma_{c,ini} = 5$, across all cases. This is primarily due to higher average Doppler factors

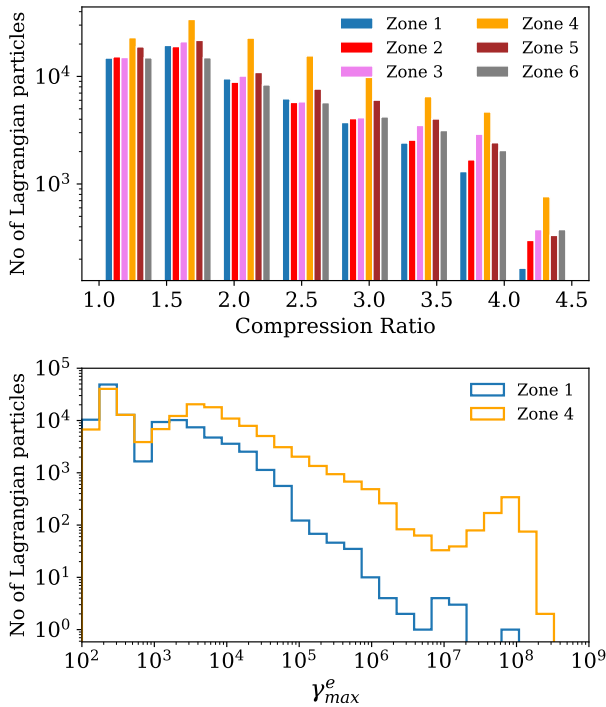


Figure 7. Histogram for the compression ratio of the last encountered shock for the Lagrangian particles inside the six zones of the jet with $\Gamma_{c,ini} = 5$ (*top panel*). Step histogram for the γ_{max} of each Lagrangian particle specifically in Zone 1 and Zone 4 of the jet with $\Gamma_{c,ini} = 5$ (*bottom panel*).

in certain zones arising from a higher initial bulk Lorentz factor.

For both jets, the multi-wavelength photon flux features two peaks - the relatively lower energy peak arising due to synchrotron emissions and the high-energy component resulting from inverse Compton scattering.

Figure 10 also depicts the prominent components for Case 4 of the multi-zone photon SED (*dotted lines*), for both the simulated jets. The SED components are calculated by combining the contributions from each zone in the jet. Different zones contribute across the frequency spectrum to varying extents, shaping the multi-zone photon flux, with certain zones dominating in specific frequency bands. Interestingly, the corresponding total multi-zone photon flux remains almost identical across all four proton distribution cases for each jet simulations. Only notable difference arises at high frequencies, where the π^0 -decay photons contribute to the total photon flux, with Case 4 exhibiting comparatively higher π^0 -decay flux. We also observe that the primary lepton synchrotron and inverse Compton components of the photon SED dominate over the hadronic counterparts. This clearly reflects the consistently low values of

the underlying proton-to-electron number density ratio η_{zone} across all six zones for our jet simulations.

The average power for the RMHD jets excluding the rest mass energy (as described in Mignone & McKinney 2007; English et al. 2016; Mukherjee et al. 2020; Upreti et al. 2024) at initial time, is estimated to be $\approx 4 \times 10^{45}$ erg s $^{-1}$ for the $\Gamma_{c,ini} = 5$ jet, and $\approx 2 \times 10^{46}$ erg s $^{-1}$ for the $\Gamma_{c,ini} = 10$ jet.

3.4. Impact of external photon fields

With an aim to study the impact of photon fields external to the jet as targets for inverse Compton emission, we conducted additional simulations for the $\Gamma_{c,ini} = 5$ jet. We refer to the simulation run considering the BLR photon field as *Ref_g5_BLR*, and the run considering the DT photon field as *Ref_g5_DT*. For the lepto-hadronic analysis we consider only Case 4 for the proton distribution where we take $\alpha^P = 2.0$ (see Table 1).

The zonal segmentation for the *Ref_g5_BLR* and *Ref_g5_DT* jets are done at the time $t_{s1} = 782$ years, similar to its $\Gamma_{c,ini} = 5$ counterpart without EC (Section 3.2). In Figure 11, we show the PL/PLEC fits for the electron distribution in each of the six spherical zones for *Ref_g5_BLR*. Due to the distance of our simulated jet segments from the external photon fields, as well as the presence of active DSA during the linear kink phase causing acceleration to be dominant at the selected time, the consideration of EC results in small to moderate modifications in the zonal electron distributions compared to the non-EC $\Gamma_{c,ini} = 5$ jet simulations. Specifically, we find that γ_{max}^e relatively decreases by $\approx 6.9 - 12\%$ in certain zones for *Ref_g5_BLR* and by $\approx 7.2 - 25\%$ in certain zones for *Ref_g5_DT*. The power-law indices for the EC simulations also exhibit small variations compared to the zones of the non-EC jet simulation.

In Figure 12 we compare the multi-zone photon and neutrino SEDs, combining contributions from each zone for the *Ref_g5_BLR* and *Ref_g5_DT* jets. For both simulations, the figure also depicts the major spectral components of the SED (combining all zonal contributions), which includes electron synchrotron emission, proton synchrotron emission, and inverse Compton scattering. Additionally, we have depicted the respective external photon fields for both the EC simulations.

Due to the distance-dependent dilution, the BLR photon field energy density becomes too weak to substantially modify the inverse Compton or neutrino components for pc scale distances. Hence, the resulting SED for *Ref_g5_BLR* closely resembles that of the $\Gamma_{c,ini} = 5$ jet without EC, in terms of the flux across different frequencies. While for *Ref_g5_DT*, we observe relatively

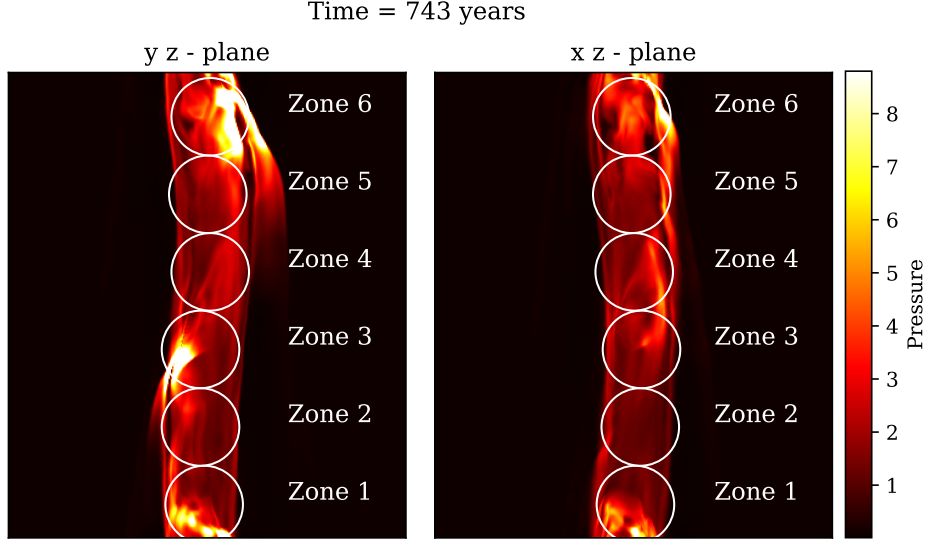


Figure 8. Slices of the yz -plane (*Left*) and the xz -plane (*Right*) with their color representing the thermal pressure (see color bar) for the jet with $\Gamma_{c,ini} = 10$ at time $t_{s2} = 743$ years.

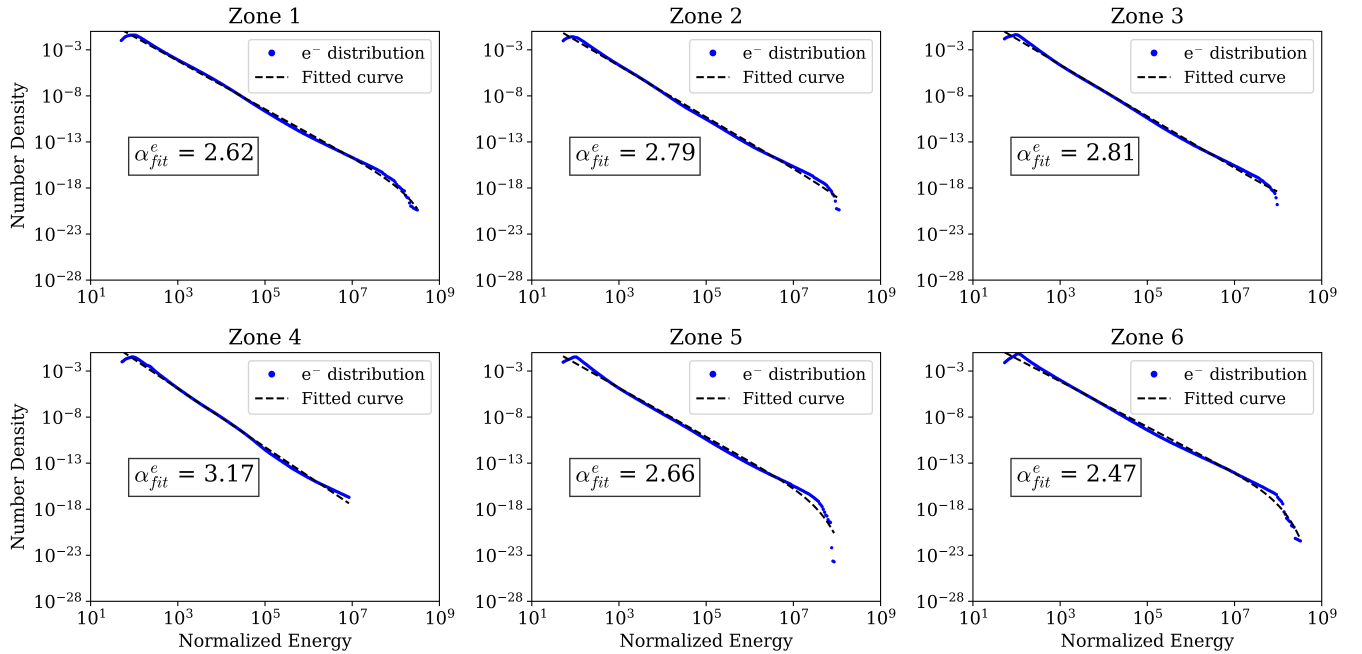


Figure 9. The respective electron distributions and the fitted PL/PLEC curve for the six zones of the jet with $\Gamma_{c,ini} = 10$ at time $t_{s2} = 743$ years.

higher IC emissions, by a factor of 2–80 across different frequencies, compared to *Ref_g5_BLR*. This is expected due to the relatively higher co-moving frame energy density provided by the DT field in the emission zones. This trend is consistent with previous studies (e.g. [Ghisellini & Tavecchio 2009](#); [Tavecchio et al. 2013](#)), which showed that the DT is the dominant radiation field at the distances of $\gtrsim 10$ pc from the central engine which is

relevant to our study. We also find modest enhancements of the total photon flux around the peak frequencies of each of the external photon fields. However, the neutrino SED remains similar for both *Ref_g5_BLR* and *Ref_g5_DT*.

4. BRIDGING SYNTHETIC EMISSION SIGNATURES WITH OBSERVATIONS

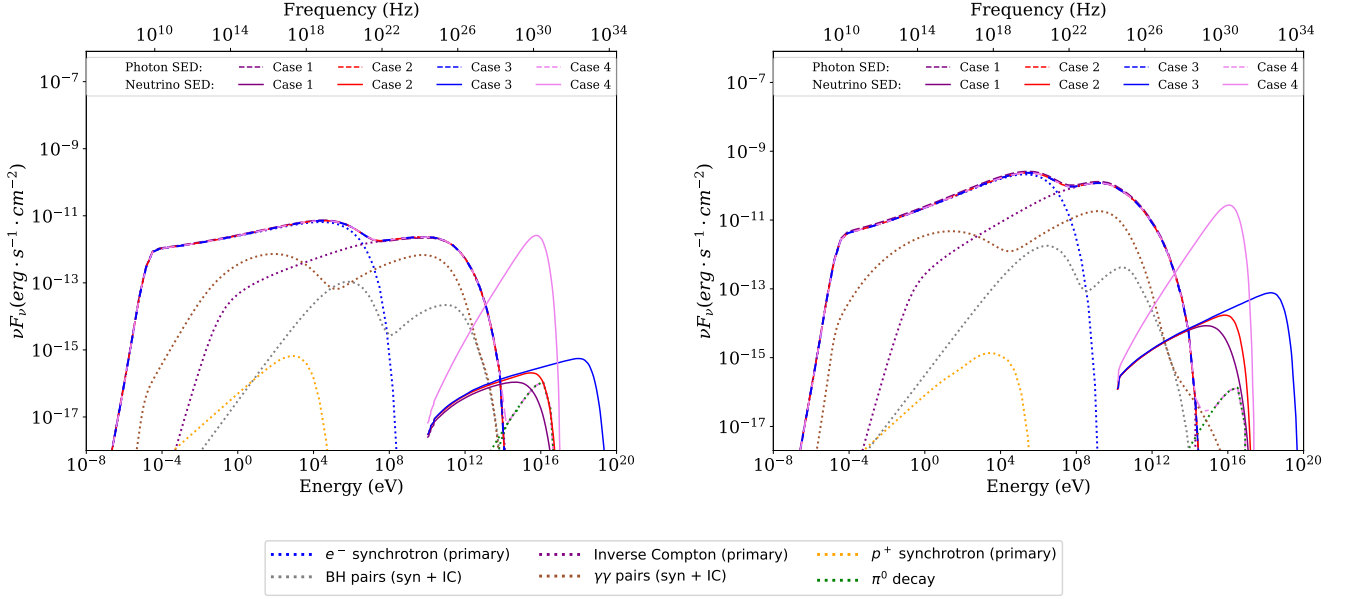


Figure 10. The Multi-zone photon (*dashed lines*) and neutrino (*solid lines*) SED for all four cases for the proton distribution for the jets with $\Gamma_{c,ini} = 5.0$ (left), and $\Gamma_{c,ini} = 10.0$ (right), respectively. The multi-zone photon SED components for Case 4 arising from different processes have been depicted using *dotted lines* (each component sums up the contributions from different zones).

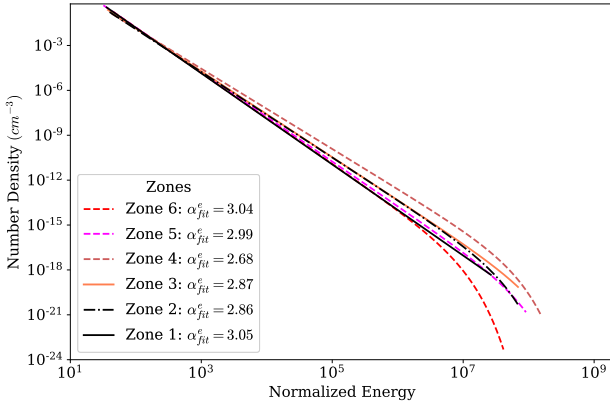


Figure 11. Electron distribution fitted curves for the 6 spherical zones of the *Ref_g5_BLR* jet.

A major objective of this study is to explore the intriguing relationship between jet composition, the onset of jet instabilities, and the emission features of AGN jets, using a computational framework for lepto-hadronic multi-zone modeling that we have developed as part of this work. We have carried out the multi-zone lepto-hadronic analysis as described in Section 2.4 and have derived the resultant synthetic photon SEDs and neutrino fluxes for a kink unstable 3D magnetized jet column. Essentially, the adopted approach greatly reduces the otherwise extensive free parameter space that would be required for multi-zone modeling. The study further aims to pave the way for connecting RMHD sim-

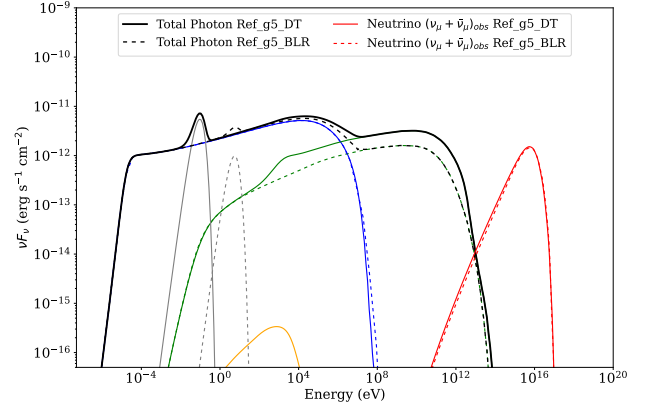


Figure 12. The multi-zone photon and neutrino SED for *Ref_g5_BLR* and *Ref_g5_DT* jets. The multi-zone SED components depicted includes: electron synchrotron emission (*blue lines*), proton synchrotron emission (*orange lines*), inverse Compton emissions (*green lines*), and the external photon field (*orange lines*). The *solid lines* are for *Ref_g5_DT* and *dashed lines* are for *Ref_g5_BLR*.

ulations of AGN jets with its multi-wavelength and neutrino emission signatures. Here, we present a discussion of the findings from our RMHD jet simulations and its synthetic SEDs alongside the observations from the well known blazar TXS 0506+056 to gain deeper insights into the underlying physics of such parsec-scale blazar jets.

4.1. Insights from synthetic multi-zone photon flux

Our jet simulations do exhibit some key similarities to features of the blazar TXS 0506+056, as indicated by VLBI studies such as Li et al. (2020) and Ros, E. et al. (2020), which describe the source as a parsec-scale relativistic, magnetized jet showing evidence of jet bending. This resembles our simulations of parsec-scale sections of relativistic, magnetized jets undergoing helical kink instabilities that result in prominent structural bending at these scales (see Figures 2, 5, and 8).

While there are studies such as Britzen et al. (2019) that suggest that such structural bending can arise from two-jet cosmic collisions, there are also simulation based studies like Tchekhovskoy & Bromberg (2016) and Barniol Duran et al. (2017) that show kink instabilities causing large scale bending in jets.

Despite some of these similarities between the TXS 0506+056 blazar and our jet simulations, there are some distinctions, notably the magnetic fields in our simulations are weaker than those inferred for TXS 0506+056 in Li et al. (2020). Additionally, the particle distribution parameters in blazar jets are poorly constrained and highly model-dependent, often relying on best-fit values within the framework of simplified one-zone models. These uncertainties, combined with limited knowledge of key physical parameters that influence the emission, inevitably introduce differences between our RMHD jet and the actual conditions in TXS 0506+056.

As such, we refrain from a direct quantitative comparison with the observational data for TXS 0506+056. Nonetheless, a rough qualitative comparison between the synthetic multi-zone SED for the simulated $\Gamma_{c,\text{ini}} = 10$ jet and observations of TXS 0506+056 during its electromagnetic flares (The IceCube Collaboration et al. 2018) reveals that their photon fluxes are of similar orders of magnitude in the optical and gamma-ray bands, and partially so in the radio band. However, the synchrotron component of the multi-zone SED from our simulated jet peaks at a significantly higher energy than that observed in TXS 0506+056. Since the synchrotron photon energy scales as $\propto \gamma^2 B$, the variation in the synchrotron peak between the synthetic multi-zone SED for the $\Gamma_{c,\text{ini}} = 10$ jet and the observed SED for TXS 0506+056 likely arises due to the potential differences in the magnetic fields as well as the differences in the maximum particle energies achieved in the jet. In particular, during the linear growth phase of the kink instability in our jet simulation, particles are accelerated to very high energies in each zone, with maximum energies reaching $\gamma_{\text{max}} \sim 10^8$ which may substantially contribute to shifting the synchrotron peak to higher energies in our synthetic SEDs.

4.2. Comparing synthetic neutrino emissions with observations for TXS 0506+056

In the subsequent discussion, we provide a qualitative comparison between the synthetic multi-zone neutrino fluxes generated across different cases of our jet simulations and the observed neutrino flux from TXS 0506+056.

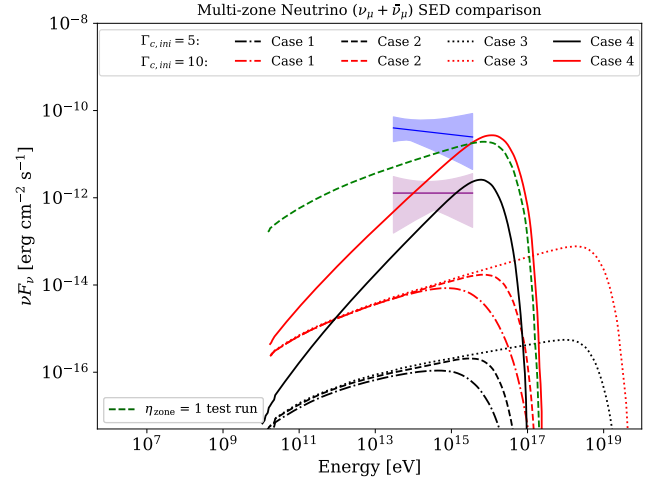


Figure 13. Multi-zone muon neutrino SEDs for the four proton distribution cases of $\Gamma_{c,\text{ini}} = 5$ (black curves) and 10 (red curves) jets. The dashed green curve represents the multi-zone neutrino flux for the test simulation with $\eta_{\text{zone}} = 1$. The blue "bow-tie" represents the best-fit muon neutrino flux (blue line) during the 110 day flaring state of TXS 0506+056 obtained by IceCube with its 68% confidence region (blue shaded region). The pink bow-tie depicts IceCube's best fit muon neutrino flux (purple line) from the 9.5 year data of TXS 0506+056 with its 68% confidence region (pink shaded region) (IceCube Collaboration 2018; Aartsen et al. 2018).

In Figure 13, we only use the IceCube data for TXS 0506+056 as a benchmark to explore whether the multi-zone muon neutrino fluxes derived from our simulated jets are of comparable magnitude and lie within an observationally relevant range, without attempting a strict quantitative fit (discussed in detail later). To understand the observational implications of these synthetic neutrino fluxes, we complement this figure by performing a calorimetric analysis that gives us a more quantitative estimate of the expected number of events that such fluxes may possibly generate in the IceCube Neutrino Observatory over different observational time periods. For the analysis, we use

$$n_{E_\nu}^{\text{exp}} = A_{\text{eff}}(E_\nu) \frac{\mathcal{F}_\nu}{E_\nu} \Delta T, \quad (25)$$

where \mathcal{F}^ν is the integrated neutrino flux, $A_{\text{eff}}(E_\nu)$ represents the effective area of the detector for a neutrino of energy E_ν arriving from a particular direction, and ΔT is the observational time interval. This estimate has been previously used in Krauß et al. (2014); Kadler et al. (2016); Kreter et al. (2020). These studies adopt an upper limit for the integrated neutrino flux by using the observed gamma-ray flux. Whereas, for our analysis, we directly utilize the synthetic neutrino flux derived from the multi-zone modeling of our simulated jets to estimate $n_{E_\nu}^{\text{exp}}$.

As specified in Table 1, for the multiple emission zone analysis of our jet simulations, we have taken 4 cases of assumptions for the proton distribution parameters. In Table 3, for both of our simulated jets we present the expected number of neutrino events $n_{E_\nu, \text{peak}}^{\text{exp}}$ for these cases, associated with the characteristic neutrino energy $E_{\nu, \text{peak}}$. We define $E_{\nu, \text{peak}}$ as the energy at which the neutrino flux for each case peaks. We calculate \mathcal{F}^ν by integrating the multi-zone muon neutrino ($\nu_\mu + \bar{\nu}_\mu$) flux over the simulated neutrino energy range. The $n_{E_\nu, \text{peak}}^{\text{exp}}$ values are computed over three observational time intervals, $\Delta T = 1, 3, 9.5$ years, respectively.

As discussed earlier, to generate the synthetic photon and neutrino emissions for our simulated jets, we have assumed the redshift and hence the luminosity distance for the jets to be identical to that of TXS 0506+056. Subsequently, considering the same sky position as TXS 0506+056 reasonably provides a basis to use the A_{eff} data provided in IceCube’s 10 year data release for TXS 0506+056 (IceCube Collaboration 2018) as representative effective areas for the $n_{E_\nu, \text{peak}}^{\text{exp}}$ calculations using the synthetic neutrino emissions from our jet simulations. We have specifically used the IC86a (May 2011- May 2012), IC86b (May 2012 - May 2015), and IC86c (May 2015 - Oct 2017) A_{eff} data provided in the data release to get a range for $n_{E_\nu, \text{peak}}^{\text{exp}}$.

Since for Case 1, we consider the proton distribution to have the same functional form (PL or PLEC) as the electron distribution in the zone, while for Case 2 the proton distribution is strictly a power-law with no exponential cutoff from cooling, we observe a relatively higher peak multi-zone neutrino flux in Case 2. Subsequently we also see a higher $n_{E_\nu, \text{peak}}^{\text{exp}}$ for Case 2 in both $\Gamma_{\text{c,ini}} = 5$ and 10 jets. On the other hand, Case 3 which again assumes a power-law with no cooling cutoff along with a higher particle γ_{max} specified by the Hillas criteria, despite having a higher peak neutrino flux than the first two cases, has a smaller $n_{E_\nu, \text{peak}}^{\text{exp}}$ as it gets scaled down by a higher $E_{\nu, \text{peak}}$.

For both jets, the expected number of events ($n_{E_\nu, \text{peak}}^{\text{exp}}$) remains below one for Cases 1, 2, and 3 across the aforementioned time intervals ΔT , implying that these fluxes may not be detectable by the current IceCube detector. However, a detector like IceCube Gen2 with a larger instrumented volume may offer enhanced sensitivity to such lower fluxes.

Only Case 4, where we assume a very flat power-law distribution for protons with an index of $\alpha^{\text{p}} = 2.0$ has a neutrino flux high enough to yield $n_{E_\nu, \text{peak}}^{\text{exp}} \geq 1$ for both jets within the observational time periods ΔT considered. Hence, suggesting that only this particular case produces a flux that may have a reasonable possibility of detection by the current IceCube detector.

This is further illustrated in Figure 13, where we have depicted the multi-zone muon neutrino flux for all the proton distribution cases corresponding to both the simulated jets. For qualitative comparison, we overlay the IceCube observational estimates from TXS 0506+056 in the form of bow-tie plots representing the best-fit muon neutrino flux and associated 68% confidence intervals for (a) the 2014–2015 flare period (from Fig. 3A in Aartsen et al. (2018)), depicted by the blue-shaded bow-tie, and (b) the 9.5-year archival excess (from Fig. 4A in Aartsen et al. (2018)), represented by the pink-shaded bow-tie.

Case 4 for both jet configurations yields synthetic fluxes that are comparable to or exceed the archival excess, while Case 4 specifically for the $\Gamma_{\text{c,ini}} = 10$ jet reaches flux levels consistent with the 2014–2015 flare scenario. Neutrino flux for the other cases are a few orders of magnitude lower than the observational estimates for TXS 0506+056.

In the synthetic SEDs that we derived for the jet simulations with no external photon field considered, we find a mismatch in the neutrino emission in the sub-PeV range as well as the neutrino spectral shape compared to the observations. Although, the flux levels in the PeV range for the favoured Case 4 scenario ($\Gamma_{\text{c,ini}} = 10$ jet) do lie within the 68% confidence region of the observed neutrino flux for the TXS 0506+056 flare.

In fact, according to literature studies (Reimer et al. 2019), reproducing the observed spectral shape for TXS 0506+056, requires a photon field (co-moving or stationary) in X-ray frequencies such that the differential photon spectrum roughly scales as $dN^{\text{ph}}/dE^{\text{ph}} \propto (E^{\text{ph}})^{-1}$ in the relevant frequency range. The relevant photon energy range to produce sub-PeV range neutrinos, for the $\delta_{\text{D}}^{\text{zone}}$ in our model, lies in soft X-rays. While we do have photons in the soft X-ray range, they scale as $dN^{\text{ph}}/dE^{\text{ph}} \propto (E^{\text{ph}})^{-2.8}$ instead of $\propto (E^{\text{ph}})^{-1}$ as found by Reimer et al. (2019) in the relevant range. This could

Table 3. Expected neutrino event counts for jets with $\Gamma_{c,\text{ini}} = 5$ and 10, for $\Delta T = 1, 3, 9.5$ years.

ΔT (years)	$n_{E_{\nu,\text{peak}}}^{\text{exp}}$ (For $\Gamma_{c,\text{ini}} = 5.0$)				$n_{E_{\nu,\text{peak}}}^{\text{exp}}$ (For $\Gamma_{c,\text{ini}} = 10.0$)			
	Case 1 ($\times 10^{-3}$)	Case 2 ($\times 10^{-3}$)	Case 3 ($\times 10^{-5}$)	Case 4	Case 1 ($\times 10^{-2}$)	Case 2 ($\times 10^{-2}$)	Case 3 ($\times 10^{-3}$)	Case 4
1	0.09–0.12	0.07–0.09	0.14–0.21	0.24–0.30	0.56–0.72	0.29–0.38	0.13–0.19	1.85–2.51
3	0.28–0.36	0.20–0.26	0.41–0.63	0.72–0.90	1.68–2.15	0.89–1.15	0.38–0.57	5.54–7.52
9.5	0.88–1.14	0.65–0.82	1.30–1.99	2.29–2.84	5.31–6.82	2.82–3.66	1.19–1.82	17.53–23.80

NOTE—Here $n_{E_{\nu,\text{peak}}}^{\text{exp}}$ denotes the expected number of neutrino events at the energy where the multi-zone neutrino flux peaks ($E_{\nu,\text{peak}}$), computed for four proton distribution cases. At the respective $E_{\nu,\text{peak}}$ for each case, the IC86a, IC86b, and IC86c A_{eff} data from the TXS 0506+056 10-year IceCube data release (IceCube Collaboration 2018) are used as representative effective areas to determine the range for each entry in the table.

be the reason for the sub-PeV range mismatch in our neutrino spectrum compared to the observations of TXS 0506+056.

As noted in Section 3.4, even with the presence of external stationary photon fields in the AGN frame, one of which is the BLR field peaking around UV to very soft X-ray frequencies, due to the distance of the modeled jet section from the BLR this external field remains subdominant to the internal co-moving photon field. While the DT field does modify the IC emissions, we do not see much of an impact on the neutrino emissions. Hence the neutrino spectral shape doesn’t change much in our synthetic SEDs even with the presence of external photon fields.

This leads us to conclude that reproducing the spectral shape of the neutrino SED that corresponds to the TXS 0506+056 flare specially in the sub-PeV frequencies, likely requires an emission region placed much closer to the external photon fields considered in our simulations. Additionally, a photon field at X-ray energies, as suggested by Reimer et al. (2019); Winter & Gao (2019), may be necessary to reproduce the exact spectral shape. However, we emphasize that our study explores the potential of kink-driven shocks within jets, in producing neutrino emissions comparable to a parsec-scale neutrino-emitting blazar source, instead of an attempt to replicate the exact emissions.

We see from the zonal electron distribution results, that the synergy between kink instability, internal shocks, and diffusive shock acceleration did not produce an electron distribution with a power-law index as flat as $\alpha^e = 2.0$ in our simulations. This indicates that the shocks formed in a RMHD scenario within our jets may not be strong enough to generate particularly flat power-law particle spectra.

Moreover, as suggested by Dubey et al. (2023, 2024), even in the presence of weaker shocks, the cumulative number of shocks encountered by a particle may also play a significant role in shaping the slope of the particle distributions within the jet.

Hence, Case 4 is indeed an extreme scenario but there is merit to such an assumption given lepto-hadronic simulation based studies modeling TXS 0506+056 like Gao et al. (2019); Petropoulou et al. (2020) have shown that a power-law with $\alpha^p = 2.0$ for protons proves to be promising for reproducing the observed neutrino flux levels for the blazar source. A similar hard spectra proton distribution with $\alpha^p = 2.0$, has also been used to successfully recreate the observed neutrino emission signatures from NGC 1068 (Das et al. 2024), as well as to simulate neutrino emission from proto-magnetar jets (Bhattacharya et al. 2023).

In lepto-hadronic models, the jet composition and the subsequent photon and neutrino emissions, depend significantly on the proton-to-electron number density ratio η_{zone} . A larger η_{zone} reflects a greater proton content in the jet, naturally giving rise to an enhanced neutrino production.

In all 4 cases for the multi-zone analysis of our jet simulations, η_{zone} is quite low, lying in the range of $\sim 0.004 - 0.010$ across different zones with the mean of the zonal electron number densities being $< n_{\text{zone}}^e > \sim 2.7 \text{ cm}^{-3}$ for the $\Gamma_{c,\text{ini}} = 5$ jet. While $\eta_{\text{zone}} \sim 0.0007 - 0.013$ and $< n_{\text{zone}}^e > \sim 3.6 \text{ cm}^{-3}$ for the $\Gamma_{c,\text{ini}} = 10$ jet. The values for these parameters are estimated with the constraints specified in Section 2.4.1.

Since only the extreme case (Case 4) produces $n_{E_{\nu,\text{peak}}}^{\text{exp}} \geq 1$ for both jets, this suggests that for our multi-zone neutrino fluxes to have a reasonable chance of detection at the IceCube detector, we either require

a flat power-law distribution for protons like in Case 4 from our low η_{zone} simulations, or alternatively have a higher proton density within the jet.

To confirm the above assertion, we did a test simulation with our multi-zone framework using $\eta_{\text{zone}} = 1$ i.e. assuming equipartition between the proton and electron number densities across all zones. For this test run, we used the parameters derived for Case 2 from the RMHD simulation for the jet with $\Gamma_{\text{c,ini}} = 10$, and performed the lepto-hadronic analysis.

The neutrino flux generated by this test run is represented by the green dashed curve in Figure 13. We find that increasing the proton-to-electron ratio η_{zone} in order to achieve an equipartition in proton and electron number densities is sufficient to produce a neutrino flux comparable to the case with the very flat power-law distribution for protons. The resultant neutrino flux from the test simulation is also comparable to the TXS 0506+056 flux during the 2014-2015 flare. This proves that just shock acceleration that does not produce a very flat particle spectra in our jets, can still produce a significant neutrino flux, comparable to the TXS 0506+056 blazar, given the jet has a higher number density of protons.

4.3. *Origin of neutrinos: Intrinsic or extrinsic?*

There are both intrinsic and extrinsic pathways to achieve the aforementioned conditions favorable to substantial neutrino production. Reconnection within the jet as well as the extensive shocks generated by jet-environment interaction could be viable mechanisms to accelerate a significant amount of protons to high energies, possibly generating proton distributions like Case 4 even with small η_{zone} values. Jet-environment interactions can manifest in several scenarios, such as the interaction of the jet with broad-line region clouds (del Palacio, S. et al. 2019), jets interacting with disk winds or stellar winds (Barkov et al. 2012), or on certain occasions, via jet-jet interactions which Britzen et al. (2019) hypothesize to be the possible origin for the 2014-2015 neutrino flare from TXS 0506+056.

Apart from producing significant dynamical consequences resulting in particle acceleration hence possibly generating a flat power-law proton distribution, such interactions can cause entrainment of proton-rich matter from the surroundings into the jet thereby enhancing the proton density within the jet. The proton distribution within each zone may then be defined as a combination

of the intrinsic and entrained components:

$$\begin{aligned} N^{\text{P}}(\gamma) &= N_{\text{int}}^{\text{P}}(\gamma) + N_{\text{ent}}^{\text{P}}(\gamma) \\ &= \frac{\eta_{\text{zone}} \rho_{\text{zone}}^{\text{NT}}}{(m_{\text{e}} + \eta_{\text{zone}} m_{\text{p}})} f_{\text{int}}(\gamma) + N_{\text{ent}}^{\text{P}}(\gamma) \end{aligned} \quad (26)$$

where $N_{\text{int}}^{\text{P}}(\gamma)$ and $N_{\text{ent}}^{\text{P}}(\gamma)$ are the intrinsic and entrained proton populations with $f_{\text{int}}(\gamma)$ being the distribution function for the intrinsic population. This additional component for entrained protons within the jet along with the associated dynamics during the jet-environment interactions can create limited periods of flaring activity in neutrino flux similar to what is observed from sources like TXS 0506+056.

To break the dichotomy between the different pathways for possible proton enrichment in the jet, we need to incorporate an actual population of protons into our simulations and study how the dynamical evolution of the jet impacts the proton distribution instead of taking phenomenological approximations for the same. Overcoming this limitation by building a module to incorporate proton macro-particles into our RMHD simulations will be a central focus of our upcoming work, as we move toward developing a more self-consistent and physically complete multi-zone framework for AGN jets and apply it to study different intrinsic and extrinsic scenarios.

5. CONCLUSIONS

The particle composition of AGN jets remains an open question since long, posing a fundamental challenge to our understanding of the dynamics of these jets and their emission mechanisms. Most of the emission zone modeling for AGN jets is typically confined to a single-zone approximation, which, however, fails to capture how a complex jet morphology and dynamics will affect the resultant multi-messenger emission.

In this work, we have followed a new, more general approach. We have first performed 3D RMHD simulations of parsec-scale AGN jet sections using the PLUTO code. The jet dynamics is then coupled to a multi-zone framework that utilizes a lepto-hadronic code (Jiménez-Fernández & van Eerten 2020) for modeling the interactions and emissions from individual zones. Our framework produces synthetic spectral energy distributions of photons and neutrinos combining the contribution from many jet emission zones. The multi-zone framework presented in this work is also tested and validated with established one-zone codes that are widely used in the community (see Appendix C).

Our framework utilizes RMHD simulations to derive quantitatively the parameters that are required for the multi-zone modeling, thus circumventing the challenge

posed by the large number of free parameters for such a model while improving upon certain simplified approximations for one-zone models. The key insights from our study can be summarized as follows.

- Our 3D RMHD simulations show that jet instabilities generate complex magnetic field configurations, naturally facilitating the formation of different emission regions across the jet. The zonal analysis of the jet simulations reveal that during the onset of instabilities, varying particle distributions emerge across these zones, translating to significant differences in their individual zonal SEDs. Emissions from different zones contribute in varying extents across different frequency bands. This highlights that single zone approximations are insufficient to capture a realistic picture of the jet.
- Our results clearly validate that proper modeling of AGN jets require a multi-zone approach - one that captures the jet dynamics capable of creating multiple emission regions across the jet, each of which can have a significant impact on the resultant multi-zone photon and neutrino SEDs.
- We find that a single-zone model yields the best-fit parameters under the assumption that majority of the jet’s emissions arise from a compact, homogeneous emission zone. However, when this assumption fails, which our simulation results and supporting studies suggest to be a likely possibility, this failure can lead to a highly biased interpretation of the underlying jet physics. We therefore conclude that a multi-zone framework is the way to go in this regard, as it can accommodate both a single zone scenario where the contribution from only one of the many zones dominate, as well as scenarios where multiple zones significantly contribute to the overall emission.
- There can be both intrinsic and extrinsic pathways for hadron enrichment in jets. The present study focuses on exploring the neutrino emissions produced through the intrinsic pathway. The zonal proton-to-electron number density ratio in our lepto-hadronic analysis are constrained to consistently low values. Under such conditions, producing a possibly detectable neutrino flux for a detector like IceCube requires an underlying proton population which is accelerated to a flat power-law having a power-law index ~ 2.0 . However, we observe in our model that intrinsic shocks generated due to the onset of kink instabilities alone, are not strong enough to produce such flat particle power-law indices for the parameters of our simulations.
- We suggest that other intrinsic mechanisms, such as magnetic reconnection within the jet, which can efficiently accelerate particles, may need to be considered to achieve the flat proton power-law spectra required to produce significant neutrino emissions. Further, shocks generated due to other intrinsic processes (apart from the kink instability) could aid in accelerating particles to high energies. This needs to be investigated in further studies.
- Alternatively, we find that increasing the value of the proton-to-electron number density ratio for the zones in the jet, even with just shock acceleration dominating, can significantly enhance the neutrino flux. It can generate flux levels comparable to the relatively flat proton power-law scenarios of our low proton-to-electron number density ratio jets. A probable pathway to achieve a higher proton number density within the jet is to account for jet-environment interactions, through which proton-rich matter from the surroundings may be entrained into the jet, a pathway we will investigate in our future work.
- Including external Compton scattering from the BLR photon field in our simulation produces only minor changes in the electron distribution and in the resulting photon and neutrino SEDs. Comparatively, including the dusty torus photon field, yields 2 – 80 times higher inverse Compton emissions across a range of frequencies, highlighting the dominance of the dusty torus photon field over the BLR field when emission zones are located at parsec-scale distances.
- In terms of potential limitations of our modeling, we note that the proton spectra are phenomenologically assumed from the leptonic spectra that is evolved as described in Section 2.2. Furthermore, the leptonic spectral evolution for each macroparticle co-moving with the jet flow is evolved without taking into account cooling due to SSC while the one-zone lepto-hadronic code used in the present study incorporates SSC process to obtain the multi-zone SED introducing a potential inconsistency. However, this discrepancy will only have a secondary impact on the scenario that is favorable for significant neutrino production. In future studies, effects due to SSC on the macroparticle spectra evolution would be incorporated with RMHD simulations.

The aim of this study was essentially to develop a tool to model and test out how different dynamical features in a jet can affect the multi-messenger emissions generated by the jet material. In a future approach, it would be essential to include the evolution of hadrons as well in order to be able to apply proton spectra that are self-consistently derived from the jet dynamics as an enhancement to our current multi-zone framework. This would further allow us to disentangle and also to quantify the role of the number density of non-thermal protons as compared to non-thermal electrons in the jet. Such a model development, whereby leptons and hadrons are evolved along with the dynamics, will require substantial coding effort and will be taken up in a subsequent study.

ACKNOWLEDGMENTS

We thank an anonymous referee for their extremely valuable suggestions that have helped to improve our paper considerably. We thank Andrea Mignone and collab-

orators for developing and providing the PLUTO code (Mignone et al. 2007), which was used for our RMHD simulations. We also acknowledge the authors of the *Katu* code (Jiménez-Fernández & van Eerten 2020), used for radiative and neutrino emission modeling. We also acknowledge the authors of the new PyPLUTO code (Mattia et al. 2025) which has been extensively used for our work. B.V. would like to acknowledge the support from the Max Planck Partner group Award established at IIT Indore. H.B. is funded by the DST INSPIRE Fellowship and acknowledges its support towards the Ph.D. H.B. also thanks Mukul Bhattacharya for the very helpful discussions. C.F. and B.V. acknowledges the support of the Deutsche Forschungsgemeinschaft (DFG, German Research Foundation), project number 443220636, via the Research Unit FOR 5195. All the simulations have been performed using the MPCDF computing clusters *Raven* and *Vera* of the Max Planck Society and the facilities provided at IIT Indore.

REFERENCES

- Aartsen, M., et al. 2018, *Science*, 361, 147–151, doi: [10.1126/science.aat2890](https://doi.org/10.1126/science.aat2890)
- Aartsen, M. G., Ackermann, M., Adams, J., et al. 2015, *Phys. Rev. Lett.*, 114, 171102, doi: [10.1103/PhysRevLett.114.171102](https://doi.org/10.1103/PhysRevLett.114.171102)
- Abbasi, R., et al. 2022, *Science*, 378, 538, doi: [10.1126/science.abg3395](https://doi.org/10.1126/science.abg3395)
- Abdo, A. A., et al. 2010, *The Astrophysical Journal*, 716, 30, doi: [10.1088/0004-637x/716/1/30](https://doi.org/10.1088/0004-637x/716/1/30)
- Acharya, S., Borse, N. S., & Vaidya, B. 2021, *Monthly Notices of the Royal Astronomical Society*, 506, 1862, doi: [10.1093/mnras/stab1775](https://doi.org/10.1093/mnras/stab1775)
- Acharya, S., Vaidya, B., Kalpa Dihingia, I., Agarwal, S., & Shukla, A. 2023, *A&A*, 671, A161, doi: [10.1051/0004-6361/202244256](https://doi.org/10.1051/0004-6361/202244256)
- Aguilar-Ruiz, E., Fraija, N., & Galván-Gómez, A. 2023, *The European Physical Journal C*, 83, doi: [10.1140/epjc/s10052-023-11523-w](https://doi.org/10.1140/epjc/s10052-023-11523-w)
- Aharonian, F. 2000, *New Astronomy*, 5, 377, doi: [https://doi.org/10.1016/S1384-1076\(00\)00039-7](https://doi.org/10.1016/S1384-1076(00)00039-7)
- Aharonian, F. A., Kelner, S. R., & Prosekin, A. Y. 2010, *PhRvD*, 82, 043002, doi: [10.1103/PhysRevD.82.043002](https://doi.org/10.1103/PhysRevD.82.043002)
- Allakhverdyan, V. A., Avrorin, A. D., Avrorin, A. V., et al. 2023, *Monthly Notices of the Royal Astronomical Society*, 527, 8784, doi: [10.1093/mnras/stad3653](https://doi.org/10.1093/mnras/stad3653)
- Ball, D., Sironi, L., & Özel, F. 2018, *The Astrophysical Journal*, 862, 80, doi: [10.3847/1538-4357/aac820](https://doi.org/10.3847/1538-4357/aac820)
- Barkov, M. V., Aharonian, F. A., Bogovalov, S. V., Kelner, S. R., & Khangulyan, D. 2012, *ApJ*, 749, 119, doi: [10.1088/0004-637X/749/2/119](https://doi.org/10.1088/0004-637X/749/2/119)
- Barniol Duran, R., Tchekhovskoy, A., & Giannios, D. 2017, *Monthly Notices of the Royal Astronomical Society*, 469, 4957, doi: [10.1093/mnras/stx1165](https://doi.org/10.1093/mnras/stx1165)
- Bhattacharya, M., Carpio, J. A., Murase, K., & Horiuchi, S. 2023, *Monthly Notices of the Royal Astronomical Society*, 521, 2391, doi: [10.1093/mnras/stad494](https://doi.org/10.1093/mnras/stad494)
- Blandford, R., Meier, D., & Readhead, A. 2019, *Annual Review of Astronomy and Astrophysics*, 57, 467, doi: <https://doi.org/10.1146/annurev-astro-081817-051948>
- Błażejowski, M., Sikora, M., Moderski, R., & Madejski, G. M. 2000, *The Astrophysical Journal*, 545, 107, doi: [10.1086/317791](https://doi.org/10.1086/317791)
- Bloom, S. D., & Marscher, A. P. 1996, *ApJ*, 461, 657, doi: [10.1086/177092](https://doi.org/10.1086/177092)
- Bodo, G., Mamatsashvili, G., Rossi, P., & Mignone, A. 2019, *Monthly Notices of the Royal Astronomical Society*, 485, 2909–2921, doi: [10.1093/mnras/stz591](https://doi.org/10.1093/mnras/stz591)
- Boettcher, M., & Schlickeiser, R. 1997, *A&A*, 325, 866, doi: [10.48550/arXiv.astro-ph/9703069](https://doi.org/10.48550/arXiv.astro-ph/9703069)
- Böttcher, M. 2019, *Galaxies*, 7, doi: [10.3390/galaxies7010020](https://doi.org/10.3390/galaxies7010020)
- Böttcher, M., & Baring, M. G. 2019, *PoS, HEASA2018*, 031. <https://arxiv.org/abs/1903.12381>

- Britzen, S., Fendt, C., Böttcher, M., et al. 2019, *Astron. Astrophys.*, 630, A103, doi: [10.1051/0004-6361/201935422](https://doi.org/10.1051/0004-6361/201935422)
- Böttcher, M., Reimer, A., Sweeney, K., & Prakash, A. 2013, *The Astrophysical Journal*, 768, 54, doi: [10.1088/0004-637X/768/1/54](https://doi.org/10.1088/0004-637X/768/1/54)
- Cerruti, M., Zech, A., Boisson, C., & Inoue, S. 2015, *Monthly Notices of the Royal Astronomical Society*, 448, 910, doi: [10.1093/mnras/stu2691](https://doi.org/10.1093/mnras/stu2691)
- Cleary, K., Lawrence, C. R., Marshall, J. A., Hao, L., & Meier, D. 2007, *The Astrophysical Journal*, 660, 117, doi: [10.1086/511969](https://doi.org/10.1086/511969)
- Das, A., Zhang, B. T., & Murase, K. 2024, *The Astrophysical Journal*, 972, 44, doi: [10.3847/1538-4357/ad5a04](https://doi.org/10.3847/1538-4357/ad5a04)
- Dedner, A., Kemm, F., Kröner, D., et al. 2002, *Journal of Computational Physics*, 175, 645, doi: [10.1006/jcph.2001.6961](https://doi.org/10.1006/jcph.2001.6961)
- del Palacio, S., Bosch-Ramon, V., & Romero, G. E. 2019, *A&A*, 623, A101, doi: [10.1051/0004-6361/201834231](https://doi.org/10.1051/0004-6361/201834231)
- Del Zanna, L., Bucciantini, N., & Londrillo, P. 2003, *A&A*, 400, 397, doi: [10.1051/0004-6361:20021641](https://doi.org/10.1051/0004-6361:20021641)
- Dermer, C. D., & Menon, G. 2009, *High Energy Radiation from Black Holes: Gamma Rays, Cosmic Rays, and Neutrinos*
- Dermer, C. D., & Schlickeiser, R. 1993, *ApJ*, 416, 458, doi: [10.1086/173251](https://doi.org/10.1086/173251)
- Diltz, C., & Böttcher, M. 2014, *Journal of High Energy Astrophysics*, 1-2, 63, doi: <https://doi.org/10.1016/j.jheap.2014.04.001>
- Dubey, R. P., Fendt, C., & Vaidya, B. 2023, *The Astrophysical Journal*, 952, 1, doi: [10.3847/1538-4357/ace0bf](https://doi.org/10.3847/1538-4357/ace0bf)
- . 2024, *The Astrophysical Journal*, 976, 144, doi: [10.3847/1538-4357/ad8135](https://doi.org/10.3847/1538-4357/ad8135)
- English, W., Hardcastle, M. J., & Krause, M. G. H. 2016, *MNRAS*, 461, 2025, doi: [10.1093/mnras/stw1407](https://doi.org/10.1093/mnras/stw1407)
- Fiorillo, D. F. G., Petropoulou, M., Comisso, L., Peretti, E., & Sironi, L. 2024, *The Astrophysical Journal Letters*, 961, L14, doi: [10.3847/2041-8213/ad192b](https://doi.org/10.3847/2041-8213/ad192b)
- Gao, S., Fedynitch, A., Winter, W., & Pohl, M. 2019, *Nature Astronomy*, 3, 88, doi: [10.1038/s41550-018-0610-1](https://doi.org/10.1038/s41550-018-0610-1)
- Gao, S., Pohl, M., & Winter, W. 2017, *The Astrophysical Journal*, 843, 109, doi: [10.3847/1538-4357/aa7754](https://doi.org/10.3847/1538-4357/aa7754)
- Garrappa, S., Buson, S., Franckowiak, A., et al. 2019, *The Astrophysical Journal*, 880, 103, doi: [10.3847/1538-4357/ab2ada](https://doi.org/10.3847/1538-4357/ab2ada)
- Ghisellini, G., & Tavecchio, F. 2008, *Monthly Notices of the Royal Astronomical Society*, 387, 1669, doi: [10.1111/j.1365-2966.2008.13360.x](https://doi.org/10.1111/j.1365-2966.2008.13360.x)
- . 2009, *Monthly Notices of the Royal Astronomical Society*, 397, 985, doi: [10.1111/j.1365-2966.2009.15007.x](https://doi.org/10.1111/j.1365-2966.2009.15007.x)
- Giannios, D. 2010, *Monthly Notices of the Royal Astronomical Society: Letters*, 408, L46, doi: [10.1111/j.1745-3933.2010.00925.x](https://doi.org/10.1111/j.1745-3933.2010.00925.x)
- Hovatta, T., & Lindfors, E. 2019, *New Astronomy Reviews*, 87, 101541, doi: <https://doi.org/10.1016/j.newar.2020.101541>
- Hümmer, S., Rügner, M., Spanier, F., & Winter, W. 2010, *The Astrophysical Journal*, 721, 630, doi: [10.1088/0004-637X/721/1/630](https://doi.org/10.1088/0004-637X/721/1/630)
- IceCube Collaboration. 2018, *IceCube data from 2008 to 2017 related to analysis of TXS 0506+056*, doi: [10.21234/B4QG92](https://doi.org/10.21234/B4QG92)
- Jerrim, L., Shabala, S., Yates-Jones, P., et al. 2025, *BRAiSE: synthetic polarisation in RMHD AGN jet simulations*, doi: [10.48550/arXiv.2506.19541](https://doi.org/10.48550/arXiv.2506.19541)
- Jiménez-Fernández, B., & van Eerten, H. J. 2020, *Monthly Notices of the Royal Astronomical Society*, 500, 3613–3630, doi: [10.1093/mnras/staa3163](https://doi.org/10.1093/mnras/staa3163)
- Jones, F. C. 1968, *Phys. Rev.*, 167, 1159, doi: [10.1103/PhysRev.167.1159](https://doi.org/10.1103/PhysRev.167.1159)
- Kadler, M., Krauß, F., Mannheim, K., et al. 2016, *Nature Physics*, 12, 807, doi: [10.1038/nphys3715](https://doi.org/10.1038/nphys3715)
- Kelner, S. R., & Aharonian, F. A. 2008, *Phys. Rev. D*, 78, 034013, doi: [10.1103/PhysRevD.78.034013](https://doi.org/10.1103/PhysRevD.78.034013)
- Khanguyan, D., Aharonian, F. A., & Kelner, S. R. 2014, *The Astrophysical Journal*, 783, 100, doi: [10.1088/0004-637X/783/2/100](https://doi.org/10.1088/0004-637X/783/2/100)
- Krauß, F., Kadler, M., Mannheim, K., et al. 2014, *A&A*, 566, L7, doi: [10.1051/0004-6361/201424219](https://doi.org/10.1051/0004-6361/201424219)
- Kreter, M., Kadler, M., Krauß, F., et al. 2020, *The Astrophysical Journal*, 902, 133, doi: [10.3847/1538-4357/abb5b1](https://doi.org/10.3847/1538-4357/abb5b1)
- Kundu, S., Vaidya, B., & Mignone, A. 2021, *The Astrophysical Journal*, 921, 74, doi: [10.3847/1538-4357/ac1ba5](https://doi.org/10.3847/1538-4357/ac1ba5)
- Li, X., An, T., Mohan, P., & Giroletti, M. 2020, *The Astrophysical Journal*, 896, 63, doi: [10.3847/1538-4357/ab8f9f](https://doi.org/10.3847/1538-4357/ab8f9f)
- Lipari, P., Lusignoli, M., & Meloni, D. 2007, *Phys. Rev. D*, 75, 123005, doi: [10.1103/PhysRevD.75.123005](https://doi.org/10.1103/PhysRevD.75.123005)
- Lister, M. L., Homan, D. C., Kellermann, K. I., et al. 2021, *The Astrophysical Journal*, 923, 30, doi: [10.3847/1538-4357/ac230f](https://doi.org/10.3847/1538-4357/ac230f)
- Lister, M. L., Cohen, M. H., Homan, D. C., et al. 2009, *The Astronomical Journal*, 138, 1874, doi: [10.1088/0004-6256/138/6/1874](https://doi.org/10.1088/0004-6256/138/6/1874)

- Liu, R.-Y., Rieger, F. M., & Aharonian, F. A. 2017, *The Astrophysical Journal*, 842, 39, doi: [10.3847/1538-4357/aa7410](https://doi.org/10.3847/1538-4357/aa7410)
- Maraschi, L., Ghisellini, G., & Celotti, A. 1992, *ApJL*, 397, L5, doi: [10.1086/186531](https://doi.org/10.1086/186531)
- Marcowith, A., Ferrand, G., Grech, M., et al. 2020, *Liv. Rev. Comput. Astrophys.*, 6, 1, doi: [10.1007/s41115-020-0007-6](https://doi.org/10.1007/s41115-020-0007-6)
- Massaro, E., Tramacere, A., Perri, M., Giommi, P., & Tosti, G. 2006, *A&A*, 448, 861, doi: [10.1051/0004-6361:20053644](https://doi.org/10.1051/0004-6361:20053644)
- Mastichiadis, A., & Kirk, J. G. 1995a, *A&A*, 295, 613
- . 1995b, *A&A*, 295, 613
- Matthews, J. H., Bell, A. R., & Blundell, K. M. 2020, *New Astronomy Reviews*, 89, 101543, doi: <https://doi.org/10.1016/j.newar.2020.101543>
- Mattia, G., Crocco, D., Melon Fuksman, D., et al. 2025, *Journal of Open Source Software*, 10, 8448, doi: [10.21105/joss.08448](https://doi.org/10.21105/joss.08448)
- Mbarek, R., & Caprioli, D. 2021, *The Astrophysical Journal*, 921, 85, doi: [10.3847/1538-4357/ac1da8](https://doi.org/10.3847/1538-4357/ac1da8)
- Medina-Torrejón, T. E., de Gouveia Dal Pino, E. M., Kadowaki, L. H. S., et al. 2021, *The Astrophysical Journal*, 908, 193, doi: [10.3847/1538-4357/abd6c2](https://doi.org/10.3847/1538-4357/abd6c2)
- Mignone, A. 2014, *Journal of Computational Physics*, 270, 784, doi: <https://doi.org/10.1016/j.jcp.2014.04.001>
- Mignone, A., Bodo, G., Massaglia, S., et al. 2007, *The Astrophysical Journal Supplement Series*, 170, 228, doi: [10.1086/513316](https://doi.org/10.1086/513316)
- Mignone, A., & McKinney, J. C. 2007, *MNRAS*, 378, 1118, doi: [10.1111/j.1365-2966.2007.11849.x](https://doi.org/10.1111/j.1365-2966.2007.11849.x)
- Mizuno, Y., Hardee, P. E., & Nishikawa, K.-I. 2011, *The Astrophysical Journal*, 734, 19, doi: [10.1088/0004-637X/734/1/19](https://doi.org/10.1088/0004-637X/734/1/19)
- Mizuno, Y., Lyubarsky, Y., Nishikawa, K.-I., & Hardee, P. E. 2009, *The Astrophysical Journal*, 700, 684, doi: [10.1088/0004-637X/700/1/684](https://doi.org/10.1088/0004-637X/700/1/684)
- . 2012, *The Astrophysical Journal*, 757, 16, doi: [10.1088/0004-637X/757/1/16](https://doi.org/10.1088/0004-637X/757/1/16)
- Mücke, A., Protheroe, R. J., Engel, R., Rachen, J. P., & Stanev, T. 2003, *Astroparticle Physics*, 18, 593, doi: [10.1016/S0927-6505\(02\)00185-8](https://doi.org/10.1016/S0927-6505(02)00185-8)
- Mukherjee, D., Bodo, G., Mignone, A., Rossi, P., & Vaidya, B. 2020, *Monthly Notices of the Royal Astronomical Society*, 499, 681, doi: [10.1093/mnras/staa2934](https://doi.org/10.1093/mnras/staa2934)
- Murase, K., Inoue, Y., & Dermer, C. D. 2014, *Phys. Rev. D*, 90, 023007, doi: [10.1103/PhysRevD.90.023007](https://doi.org/10.1103/PhysRevD.90.023007)
- Nigro, C., Sitarek, J., Gliwny, P., et al. 2022, *A&A*, 660, A18, doi: [10.1051/0004-6361/202142000](https://doi.org/10.1051/0004-6361/202142000)
- Omeliukh, A., et al. 2025, *Astron. Astrophys.*, 695, A266, doi: [10.1051/0004-6361/202452143](https://doi.org/10.1051/0004-6361/202452143)
- O’Neill, S. M., Beckwith, K., & Begelman, M. C. 2012, *Monthly Notices of the Royal Astronomical Society*, 422, 1436, doi: [10.1111/j.1365-2966.2012.20721.x](https://doi.org/10.1111/j.1365-2966.2012.20721.x)
- Petropoulou, M., Dimitrakoudis, S., Padovani, P., Mastichiadis, A., & Resconi, E. 2015, *Monthly Notices of the Royal Astronomical Society*, 448, 2412, doi: [10.1093/mnras/stv179](https://doi.org/10.1093/mnras/stv179)
- Petropoulou, M., Giannios, D., & Dimitrakoudis, S. 2014, *Mon. Not. Roy. Astron. Soc.*, 445, 570, doi: [10.1093/mnras/stu1757](https://doi.org/10.1093/mnras/stu1757)
- Petropoulou, M., Murase, K., Santander, M., et al. 2020, *The Astrophysical Journal*, 891, 115, doi: [10.3847/1538-4357/ab76d0](https://doi.org/10.3847/1538-4357/ab76d0)
- Plavin, A., Kovalev, Y. Y., Kovalev, Y. A., & Troitsky, S. 2020, *ApJ*, 894, 101, doi: [10.3847/1538-4357/ab86bd](https://doi.org/10.3847/1538-4357/ab86bd)
- Plavin, A. V., Kovalev, Y. Y., Kovalev, Y. A., & Troitsky, S. V. 2021, *The Astrophysical Journal*, 908, 157, doi: [10.3847/1538-4357/abceb8](https://doi.org/10.3847/1538-4357/abceb8)
- . 2023, *Monthly Notices of the Royal Astronomical Society*, 523, 1799, doi: [10.1093/mnras/stad1467](https://doi.org/10.1093/mnras/stad1467)
- Reimer, A., Böttcher, M., & Buson, S. 2019, *The Astrophysical Journal*, 881, 46, doi: [10.3847/1538-4357/ab2bff](https://doi.org/10.3847/1538-4357/ab2bff)
- Ros, E., Kadler, M., Perucho, M., et al. 2020, *A&A*, 633, L1, doi: [10.1051/0004-6361/201937206](https://doi.org/10.1051/0004-6361/201937206)
- Rossi, P., Mignone, A., Bodo, G., Massaglia, S., & Ferrari, A. 2008, *Astronomy and Astrophysics*, 488, doi: [10.1051/0004-6361:200809687](https://doi.org/10.1051/0004-6361:200809687)
- Sahakyan, N., Giommi, P., Padovani, P., et al. 2022, *Monthly Notices of the Royal Astronomical Society*, 519, 1396, doi: [10.1093/mnras/stac3607](https://doi.org/10.1093/mnras/stac3607)
- Schlickeiser, R., & Ruppel, J. 2010, *New Journal of Physics*, 12, 033044, doi: [10.1088/1367-2630/12/3/033044](https://doi.org/10.1088/1367-2630/12/3/033044)
- Striani, E., Mignone, A., Vaidya, B., Bodo, G., & Ferrari, A. 2016, *Monthly Notices of the Royal Astronomical Society*, 462, 2970, doi: [10.1093/mnras/stw1848](https://doi.org/10.1093/mnras/stw1848)
- Tavecchio, F., Pacciani, L., Donnarumma, I., et al. 2013, *Monthly Notices of the Royal Astronomical Society: Letters*, 435, L24, doi: [10.1093/mnrasl/slt087](https://doi.org/10.1093/mnrasl/slt087)
- Tchekhovskoy, A., & Bromberg, O. 2016, *Monthly Notices of the Royal Astronomical Society: Letters*, 461, L46, doi: [10.1093/mnrasl/slw064](https://doi.org/10.1093/mnrasl/slw064)
- The IceCube Collaboration, Fermi-LAT, MAGIC, et al. 2018, *Science*, 361, eaat1378, doi: [10.1126/science.aat1378](https://doi.org/10.1126/science.aat1378)
- Tramacere, A., Giommi, P., Perri, M., Verrecchia, F., & Tosti, G. 2009, *A&A*, 501, 879, doi: [10.1051/0004-6361/200810865](https://doi.org/10.1051/0004-6361/200810865)

- Tramacere, A., Massaro, E., & Taylor, A. M. 2011, *ApJ*, 739, 66, doi: [10.1088/0004-637X/739/2/66](https://doi.org/10.1088/0004-637X/739/2/66)
- Upreti, N., Vaidya, B., & Shukla, A. 2024, *Journal of High Energy Astrophysics*, 44, 146, doi: <https://doi.org/10.1016/j.jheap.2024.09.007>
- Urry, C. 1999, *Astroparticle Physics*, 11, 159, doi: [https://doi.org/10.1016/S0927-6505\(99\)00043-2](https://doi.org/10.1016/S0927-6505(99)00043-2)
- Vaidya, B., Mignone, A., Bodo, G., Rossi, P., & Massaglia, S. 2018, *The Astrophysical Journal*, 865, 144, doi: [10.3847/1538-4357/aadd17](https://doi.org/10.3847/1538-4357/aadd17)
- Walker, R. C., Hardee, P. E., Davies, F. B., Ly, C., & Junor, W. 2018, *The Astrophysical Journal*, 855, 128, doi: [10.3847/1538-4357/aaafcc](https://doi.org/10.3847/1538-4357/aaafcc)
- Winter, W., & Gao, S. 2019, in *International Cosmic Ray Conference*, Vol. 36, 36th International Cosmic Ray Conference (ICRC2019), 1032, doi: [10.22323/1.358.01032](https://doi.org/10.22323/1.358.01032)
- Xue, R., Liu, R.-Y., Petropoulou, M., et al. 2019, *The Astrophysical Journal*, 886, 23, doi: [10.3847/1538-4357/ab4b44](https://doi.org/10.3847/1538-4357/ab4b44)
- Xue, R., Liu, R.-Y., Wang, Z.-R., Ding, N., & Wang, X.-Y. 2021, *The Astrophysical Journal*, 906, 51, doi: [10.3847/1538-4357/abc886](https://doi.org/10.3847/1538-4357/abc886)
- Zacharias, M., Reimer, A., Boisson, C., & Zech, A. 2022, *Monthly Notices of the Royal Astronomical Society*, 512, 3948, doi: [10.1093/mnras/stac754](https://doi.org/10.1093/mnras/stac754)
- Zuber, K. 2020, *Neutrino Physics*, doi: [10.1201/9781315195612](https://doi.org/10.1201/9781315195612)

APPENDIX

A. INITIAL PROFILES FOR JET SIMULATIONS AND MULTI-ZONE PARAMETERS

For the initial profiles of the different MHD variables in our jet simulations, we adopt the steady-state axisymmetric solutions in cylindrical coordinates for the ideal RMHD equations from [Bodo et al. \(2019\)](#). Here, for convenience, we provide the profiles of the important dynamical quantities. These profiles have been obtained by ensuring that the initial plasma column is in radial equilibrium.

The radial profile for the azimuthal velocity is expressed as follows,

$$v_\phi^2 = \frac{r^2 \Gamma_c^2 \Omega_c^2}{\Gamma_z^2 [1 + r^2 \Gamma_c^2 \Omega_c^2 \exp(-r^4/a^4)]} \exp\left(-\frac{r^4}{a^4}\right), \quad (\text{A1})$$

where r is the cylindrical radius and the characteristic concentration radius for the electric current in the jet is taken as $a = 0.6$. The initial magnetic field configuration with a pitch parameter $\mathcal{P} = rB_z/B_\phi$ is defined as,

$$B_z^2 = B_{zc}^2 - (1 - \alpha) H_c^2 \sqrt{\pi} a^{-2} \operatorname{erf}\left(\frac{r^2}{a^2}\right), \quad (\text{A2})$$

$$B_\phi = \frac{-v_\phi v_z B_z \mp \sqrt{v_\phi^2 B_z^2 + H^2(1 - v_z^2)}}{1 - v_z^2}, \quad (\text{A3})$$

where B_z and B_ϕ are the poloidal and the toroidal magnetic fields, respectively, while the radial field component is $B_r = 0$. With B_{zc} we denote the poloidal magnetic field along the central axis, erf is the error function, and H is defined as $H^2 = B_\phi^2 - E_r^2 = [1 - \exp(-r^4/a^4)] H_c^2 / r^2$ where H_c is the value of H along the central axis and $E_r = v_z B_\phi - v_\phi B_z$. We take $\alpha = 1$ where the parameter α represents the strength of rotation for the flow.

Using the aforementioned variable profiles, as well as the setup and initial conditions specified in Section 2, the RMHD jet simulations were carried out.

B. DETAILS OF THE EC SIMULATIONS

For the EC simulations considering BLR (*Ref_g5_BLR*) and DT (*Ref_g5_DT*) as the respective external photon fields, the adopted dilution factor is motivated by [Khangulyan et al. \(2014\)](#). We approximate the BLR to be a spherical photon field with a characteristic radius of $R_{\text{BLR}}^{\text{AGN}}$ from the SMBH, while we consider the DT to be an annular ring at a characteristic radius $R_{\text{DT}}^{\text{AGN}}$ (at the midpoint of the annulus). $R_{\text{BLR}}^{\text{AGN}}$

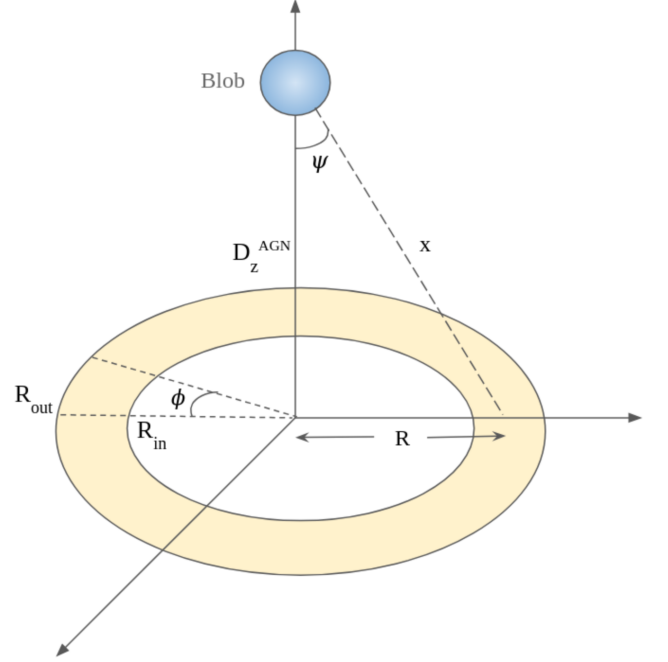


Figure 14. Illustration of the geometry used for dusty Torus.

and $R_{\text{DT}}^{\text{AGN}}$ scale proportional to $(L_{\text{disc}}^{\text{AGN}})^{1/2}$ as defined in [Ghisellini & Tavecchio \(2008\)](#). Considering an emission zone at a distance D_z^{AGN} , the dilution factor multiplied to the AGN frame energy density for BLR photon field can be expressed as,

$$\kappa_{\text{BLR}}^{\text{AGN}} = \frac{\Delta\Omega}{4\pi} = \frac{(R_{\text{BLR}}^{\text{AGN}})^2}{4(D_z^{\text{AGN}})^2}, \quad (\text{B4})$$

considering $D_z^{\text{AGN}} \gg R_{\text{BLR}}^{\text{AGN}}$.

For the DT photon field, distance of the zone from any point on the Dusty torus is $x \approx [(R)^2 + (D_z^{\text{AGN}})^2]^{1/2}$ (R is the radial distance to the DT element), and

$$d\Omega = \frac{\cos\psi}{x^2} dA = \frac{(D_z^{\text{AGN}}/x)}{x^2} (R d\phi dR), \quad (\text{B5})$$

where ψ is the angle between D_z^{AGN} and x . Doing the necessary integrations and approximating for $D_z^{\text{AGN}} \gg R_{\text{DT}}$, the corresponding dilution factor can be expressed as ⁶

$$\kappa_{\text{DT}}^{\text{AGN}} = \frac{\Delta\Omega}{4\pi} \approx \frac{R_{\text{out}}^2 - R_{\text{in}}^2}{4(D_z^{\text{AGN}})^2} \approx \frac{(R_{\text{DT}}^{\text{AGN}})^2}{2(D_z^{\text{AGN}})^2} \quad (\text{B6})$$

⁶ We take inner and outer radius of DT to be $R_{\text{in}} \approx R_{\text{DT}}^{\text{AGN}} - (R_{\text{DT}}^{\text{AGN}}/2)$ and $R_{\text{out}} \approx R_{\text{DT}}^{\text{AGN}} + (R_{\text{DT}}^{\text{AGN}}/2)$

The dilution factor provides an effective estimate of the target photon field available for inverse-Compton scattering at the emission site, by rescaling the photon field energy density, accounting for the external photon field geometry and its separation from the dissipation region. For computational simplicity, we treat the resulting photon field as a geometrically diluted but isotropic radiation field and use the corresponding Lorentz transformation (as described in Equation (A.9) in Nigro, C. et al. (2022)). A full anisotropic treatment of EC scattering however, is currently out of scope for this work.

C. SED TESTS

To validate the multi-zone framework algorithm (Section 2.4), it is necessary to first confirm that the SEDs generated for the individual zones following this algorithm are accurate. In particular, we want to corroborate that extracting average fluid parameters and the net electron distribution from the RMHD simulations for a given zone and using them as inputs to a one zone lepto-hadronic (OZLH) code, can produce viable SEDs for individual emission zones. A detailed consistency test of the inverse Compton component for a spherical blob will be presented in a subsequent work (Sharma et. al. - *In prep*).

We perform two test simulations with different initial conditions:

1. **blob simulation** - In this test, the blob is initialized with an initial uniform bulk Lorentz factor of $\Gamma_{\text{blob}} = 10$ inside the sphere with velocity of the form $v = (0, 0, v_z)$. The blob has a homogeneous poloidal magnetic field along z-axis with a magnitude of $B_{z,\text{blob}} = 2.92 \times 10^{-2}$ G and has a density contrast of $\rho_{\text{blob}}/\rho_{\text{amb}} = 10^{-3}$ where $\rho_{\text{blob}} = \rho_0 = 1.661 \times 10^{-26}$ g cm $^{-2}$. Its Doppler factor is $\delta_{\text{blob}} \approx 19.36$ with $\theta_{\text{los}} = 1^\circ$. The blob has a radius $r_{\text{blob}} = 1$ pc in a simulation domain with spatial extents of $x \in [-L_x, L_x]$, $y \in [-L_y, L_y]$, $z \in [0, L_z]$ where $L_x = L_y = L_z = 10 l_b = 10$ pc with a domain spatial grid resolution of $(400 \times 400 \times 200)$. The net electron distribution inside the blob is a perfect power-law with an index of $\alpha^e = 2.4$, $\gamma_{\text{min}}^e = 10^2$, and $\gamma_{\text{max}}^e = 10^8$.
2. **zone simulation** - This test is performed for a spherical zone taken at the base of the $\Gamma_{c,\text{ini}} = 10$ jet simulation at time $t = 743$ years. This zone has non uniform density, an average zonal magnetic field of $B_{\text{zone}} \approx 2.46 \times 10^{-2}$ G, and average Doppler factor $\delta_{\text{zone}} \approx 2.43$ with $\theta_{\text{los}} = 1^\circ$. The net electron distribution for the zone, obtained from Equation 19 is fitted with a PLEC

distribution having $\alpha_{\text{fit}}^e = 2.62$, $\gamma_{\text{min}}^e = 50.5$, $\gamma_{\text{max}}^e = 3.09 \times 10^8$ and $\gamma_{\text{break}}^e = 8.19 \times 10^7$.

For the *blob* and the *zone* simulations, we assume the proton-to-electron number density ratio to be very small, $\eta_{\text{zone}} = 10^{-33}$, since we are only interested in generating the electron synchrotron component.

In Figure 15 (*top panel*), we compute the synthetic synchrotron SEDs for the *blob* simulations for different codes typically used for OZLH modeling for AGN jets like *Katu* (Jiménez-Fernández & van Eerten 2020), *agnpy* (Nigro, C. et al. 2022) and compare with the synthetic synchrotron SED obtained from hybrid PLUTO simulations (Vaidya et al. 2018). The fluxes in these simulations are obtained using the formulations provided in (Dermer & Menon 2009; Aharonian et al. 2010). We see that in the *blob* simulation, the electron distribution has an almost perfect power-law fit and uniform Doppler factors across all cells, the resultant synchrotron SED from *Katu* and *agnpy* match very well with the synthetic PLUTO SED.

The *bottom panel* of Figure 15, we compare the synthetic synchrotron SEDs generated from *zone* simulations. Here, synthetic SEDs obtained from OZLH codes like *Katu* and *Tramacere* (Massaro et al. 2006; Tramacere et al. 2009, 2011) are compared with the SED obtained from hybrid PLUTO simulation. We observe that the SED from PLUTO (red dots) deviates for certain points from the SEDs made with the OZLH codes. At the low frequency $\nu \lesssim 10^{11}$ Hz, the deviation is primarily due to absence of synchrotron self absorption (SSA) in the hybrid PLUTO framework. Further, as the hybrid PLUTO framework, uses the exact spectra to compute the SED instead of a fitted one, we see slight deviations from those obtained from OZLH codes which uses a well-defined functional form for particle distribution.

Additionally, there are turbulent signatures within the zones which leads to variations in the Doppler factor, causing the emissivity from different parts of the zone being boosted somewhat differently. In contrast, the SEDs produced by OZLH codes assume a uniform Doppler factor, which we determine by computing a weighted average within the zone. Such an approximation results in some mismatch, between the flux generated using PLUTO which can resolve the variations within the zone, and the OZLH codes which assumes a uniform zone.

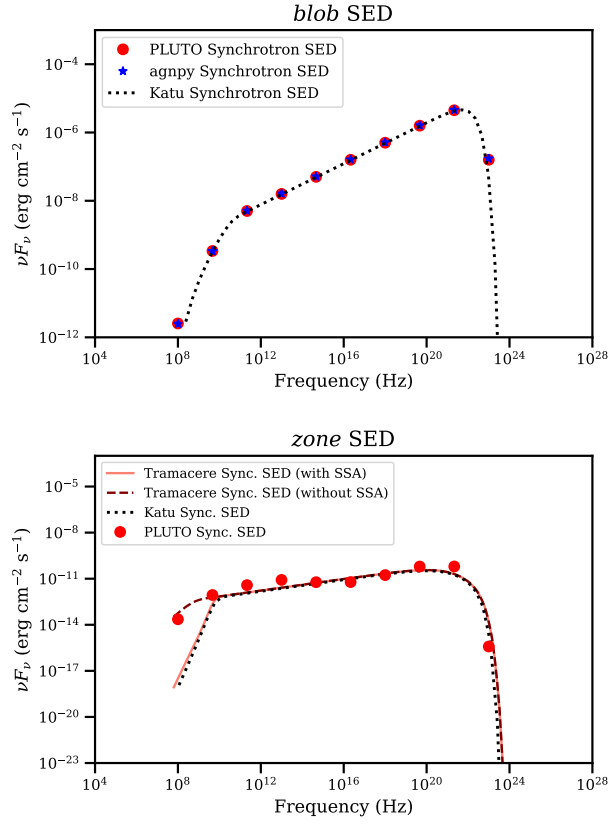


Figure 15. *Top panel:* Comparison of synchrotron SEDs for the *blob* simulations generated by PLUTO's particle module (red dots), *Katu* (black dashed) and the *agnpy* (blue star). *Bottom panel:* Synchrotron SED comparison for the *zone* simulations generated by PLUTO's particle module (red dots), *Katu* (black dashed), and the *Tramacere* tool (orange solid for with SSA, and brown dashed for without SSA case). Note, the OLZH code *Katu* also accounts for SSA.